Jet-Stirred Reactor Study of Low-Temperature Neopentane Oxidation: A Combined Theoretical, Chromatographic, Mass Spectrometric, and PEPICO Analysis

Jérémy Bourgalais, Olivier Herbinet, Hans-Heinrich Carstensen, Janney Debleza, Gustavo Garcia, Philippe Arnoux, Luc Sy Tran, Guillaume Vanhove, Binzhi Liu, Zhandong Wang, et al.

Published in Energy & Fuels
https://doi.org/10.1021/acs.energyfuels.1c02080

Jet-Stirred Reactor Study of Low-Temperature Neopentane Oxidation: A Combined Theoretical, Chromatographic, Mass Spectrometric, and PEPICO Analysis

Jérémy Bourgalais[1*], Olivier Herbinet[1], Hans-Heinrich Carstensen[2,3], Janney Debleza[1], Gustavo A. Garcia[4], Philippe Arnoux[1], Luc Sy Tran[5], Guillaume Vanhove[5], Binzhi Liu[6], Zhandong Wang[6], Majdi Hochlaf[7], Laurent Nahon[4], Frédérique Battin-Leclerc[1]

[1]LRGP, Université de Lorraine, CNRS; 1 rue Grandville, 54000 Nancy, France.
[2]Thermochemical Processes Group (GPT), Department of Chemical and Environmental Engineering, Engineering and Architecture School, University of Zaragoza, C. de Mariano Esquillor Gómez, 50018 Zaragoza, Spain.
[3]Fundacion Agencia Aragonesa para la Investigacion y el Desarrollo (ARAID), Av. de Ranillas 1-D 50018 Zagaroza, Spain.
[4]Synchrotron SOLEIL, L'Orme des Merisiers, Saint-Aubin-BP 48, 91192 Gif-sur-Yvette Cedex, France
[5]PC2A, Université de Lille, CNRS; Avenue Mendeleiev, 59650 Villeneuve-d'Ascq, France
[6]National Synchrotron Radiation Laboratory, University of Science and Technology of China, Hefei, Anhui 230029, People's Republic of China
[7]Université Gustave Eiffel, COSYS/LISIS; 5 Bd Descartes 77454, Champs sur Marne, France

Abstract

The oxidation of neopentane was studied in jet-stirred reactors at atmospheric pressure over a temperature range 500 - 850 K and ϕ = 0.5. The products were analyzed with chromatographic, mass spectrometric, and photoelectron spectroscopic setups complemented with theoretical calculations. This combination provides a comparison of photoionization mass spectrometry and gas chromatography for the quantification of mole fractions and highlights the relevant differences between them, while mass-tagged photoelectron spectroscopy sheds light onto the isomeric distribution. The new data and corresponding analyses are expected to provide valuable guidance for an extension of the kinetic model and the choice of experimental methods.

The main first and second O_2-addition products were observed in agreement with the literature (e.g., 3,3-dimethyloxetane, acetone, isobutene, and γ-ketohydroperoxide). The simulated mole fractions of the products using a literature kinetic model were compared to the experimental results. Even though the kinetic model has been validated previously, significant discrepancies between the measured and simulated mole fractions of 2-methylpropanal and methacrolein, two fuel-specific low-temperature oxidation products, were found. Furthermore, some experimentally observed species related to γ-ketohydroperoxide decomposition were not predicted indicating that the model is incomplete. The detection of 2-methylpropanal and formic acid highlighted the importance of the Korcek-type pathway.

*corresponding author: jeremy.bourgalais@univ-lorraine.fr

TOC graphic

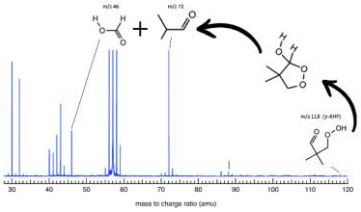

Introduction

Understanding the chemistry of auto-ignition of a fuel-air mixture, especially at low temperature (< 1,000 K) is mandatory for the design and optimization of low-emission and high-efficiency internal combustion engines (ICEs). The low-temperature oxidation of hydrocarbon fuels is governed by successive additions of radicals to O_2, intramolecular migration reactions of H-atoms, and bimolecular dissociation channels leading to chain branching or propagation. This chemistry leads to the formation of numerous oxygenated intermediates among which hydroperoxides play an important role because the reactivity of the hydroperoxides is central to auto-ignition in ICEs. The overall mechanism for low-temperature combustion of hydrocarbon fuels is relatively well understood and implemented in detailed chemical kinetic models, but quantitative agreement between measurements and simulations is not always achieved. One reason for this is that not all products formed during low temperature oxidation have unequivocally been identified[1].

Given its unique highly symmetric molecular structure, neopentane (C_5H_{12}) is an ideal candidate to study the oxidation chemistry of alkanes. With all the primary H atoms being equivalent, only one type of alkyl radical is formed in H abstraction reactions. Similarly, the initiation through C-C bond scission leads only to one set of products (methyl and *tert*butyl radicals). These limited consumption pathways for neopentane restrict the diversity of initial product channels compared to other pentane isomers. Nevertheless, successive reactions, especially O_2-addition, lead to large variety of oxygenated species through isomerization and dissociation reactions including intermediates and reactive species such as free radicals, which play a crucial role in the formation of ketohydroperoxides (KHPs). KHPs are chain branching agents, which contain carbonyl (C=O) and hydroperoxy (-OOH) functional groups. Their thermal decomposition promotes the release of OH radicals as well as other reactive species, which increase the reactivity of a combustible mixture.

Numerous studies in the literature have investigated the oxidation chemistry of neopentane in static low pressure reactors[2–7], rapid compression machines, shock tubes[8–12], as well as in flow tubes[13–17] and in jet-stirred reactors (JSR)[18–20]. These techniques allowed the identification of primary and secondary products over a temperature range from 550 K to 1,718 K. The analysis of these measurements was supported by ab initio calculations[21] and the development of chemical kinetic models[14,18,22]. Predictions in particular with the most recent model are generally good but significant discrepancies on specific species such as 2-methylpropanal suggest that some chain-branching reactions might be missing. KHPs have not been observed until very recently by Eskola et al.[17] in time-resolved, Cl-atom initiated neopentane oxidation experiments. Using a synchrotron photoionization time-of-flight mass spectrometer, the KHP 3-hydroperoxy-2,2-dimethylpropanal was identified and its decomposition mechanisms explored. Based on some oxidation products found in neopentane oxidation, Eskola et al.[17] suggested that 3-hydroperoxy-2,2-dimethylpropanal, undergoes the so-called Korcek reaction[23]. The KHP in neopentane oxidation was also

*corresponding author: jeremy.bourgalais@univ-lorraine.fr

observed by Hansen et al.[20] in a JSR and its maximum mole fraction was measured at T = 590 K. However, their work focused on the products of the third O_2-addition rather than the elementary steps leading to KHP formation and decomposition. The only other known JSR study of neopentane oxidation was performed by Dagaut et al.[18] over a temperature range from 800 K to 1,230 K, which is however not favorable for KHP formation.

This current work studies the oxidation of neopentane in a JSR in the T = 500 K - 850 K temperature range in order to identify and quantify the main oxidation products up to KHP formation and decomposition. Three JSR setups were used, each connected to different analytic equipment. The aim of this collaborative effort is twofold. First, to generate redundant data to validate the different quantification procedures used or to identify cases for which these methods lead to notable differences. Second, to generate a comprehensive data set for neopentane oxidation to provide a challenge for existing models and by doing so to enhance the current understanding of this chemistry. The three analytic systems used are:

(1) On-line gas chromatography (GC) at LRGP (Nancy, France) by connecting the outline of the JSR to two GC analyzers[24]. This setup allows to measure mole fractions as a function of temperature for neopentane, stable intermediates, and final products as a function of temperature.

(2) Time-of-flight mass spectrometry analysis using tunable synchrotron vacuum ultraviolet for photoionization (SVUV-PIMS) at the NSRL synchrotron (Hefei, China) by sampling the reaction mixture in the JSR through the formation of a molecular beam[25]. This device provides mass-resolved photoion yield (PIY) curves. The spectra are converted with the help of internal standards to species mole fractions. This device is able to detect intermediates that cannot be detected by GC analysis and therefore complementary data.

(3) Photoelectron photoion coincidence spectroscopy using tunable synchrotron vacuum ultraviolet light from the VUV DESIRS beamline at the SOLEIL synchrotron (Saint-Aubin, France) for photoionization (SVUV-PEPICO) of molecular beam sampled reaction mixture extracted from a JSR[26]. This facility allows the acquisition of mass-resolved slow photoelectron spectra (SPES)[27,28] on top of PIY, which provide information on the isomeric structures of oxidation products.

The SPES analyses are supported by high-level theoretical quantum calculations which provide simulated PES of molecular species, for which such spectra are not yet reported in the literature[26,29]. The detailed kinetic model developed at the Combustion Chemical Centre of the National University of Ireland (Galway, Ireland)[11] has been used to simulate the current neopentane experiments and to identify the major oxidation products and their dominant formation/decomposition pathways.

This paper is organized as follows. The first section presents the different experimental setups that were used as well as the theoretical methods employed to support the experimental data analysis. The kinetic model from the literature, used to simulate the chemistry of neopentane oxidation, is also briefly described. In the second section, the experimental results are presented according to the molecular growth pathway leading to the formation and decomposition of KHP. Throughout this section, the results are compared to the predictions of the used kinetic model and to available experimental results from the literature. The last section summarizes the main results of this study and proposes perspectives to improve the kinetic models for alkane oxidation at low temperature.

*corresponding author: jeremy.bourgalais@univ-lorraine.fr

Experimental facilities, theoretical methods, and kinetic model

Neopentane oxidation was studied under steady state and atmospheric pressure conditions at the equivalence ratio (ϕ) of 0.5. The flow rates were adjusted at each temperature to achieve a τ = 3 s residence time in the JSR. He and O_2 were provided by Messer in LRGP (both 99.999 % pure) and by Air Liquide at SOLEIL. Ar and O_2 were provided by Air Liquide in NSRL with a purity of 99.999 %. The LRGP and SOLEIL experiments used a neopentane mixture provided by Air Liquide with a 3% dilution in He. The purity of neopentane was found to be > 99 % based on GC analysis and was used without further purification. NSRL experiments used liquid neopentane supplied by Nanjing Special Gas Factory Co. Ltd. with a claimed purity of 99.8 %. The purity was also verified by GC analysis. Calibrated mass flow controllers were used to measure gas flow rates with a 0.5 % uncertainty. A Coriolis flow controller was used in the NSRL facility to control the fuel liquid flow rate.

JSR experiments

The experiments at LRGP and NSRL allowed obtaining mole fraction profiles of products and reactants over a wide temperature range. The measurement campaign at the SOLEIL synchrotron focused on recording SPES of species at specific temperatures near the peak mole fraction of KHP. Experiments at SOLEIL were also performed without O_2 to study the stability of neopentane during photoionization to discriminate oxidation products and dissociative ionization fragments in SPES. The experimental conditions used at the three locations are summarized in Table 1.

					mole fractions		
Location	T(K)	P(Bar)	τ(s)	ϕ	neopentane	O_2	He/Ar
NSRL	500 – 825	1.07	3	0.5	0.015	0.24	0.745
LRGP	500 – 850	1.07	3	0.5	0.015	0.24	0.745
SOLEIL	580 – 650	1.07	3	0.5	0.015	0.24	0.745
	580	1.07	3	∞	0.015	0	0.985

Table 1. Summary of JSR experimental conditions used in the present study.

JSR coupled to GC-TCD/FID/MS

The JSR used to investigate neopentane oxidation at LRGP is a fused silica spherical reactor (~81.2 cm^3) working under isothermal and isobaric conditions with a reactive gas mixture (fuel + O_2) continuously flowing into it, with a high dilution of inert gas to avoid temperature gradients due to the oxidation exothermicity. Reactants (neopentane and O_2), with helium as the carrier gas, entered the spherical JSR through four cross-shaped nozzles positioned at the center to promote turbulence and mixture homogenization. The JSR has a preheating zone upstream of the reactor inlet to reduce the temperature gradient inside of it. The JSR and the preheating zone are heated using resistances, and the reactor temperature was measured with a K-type thermocouple positioned in a glass finger close to the JSR center with an uncertainty of around 1%. The oxidation gas mixture exiting the JSR is transferred, via heated lines, to two GCs for analysis. **The length of the heating lines is ~5m of 1/8 in outside diameter stainless tube.**

The first GC is equipped with a Carbosphere-packed column and a thermal conductivity detector (TCD) to quantify lightweight and permanent gas species. The second GC is equipped with a Q-Bond capillary column and a flame ionization detector (FID) preceded by a methanizer. This GC is used for the quantification of organic compounds. The methanizer is

*corresponding author: jeremy.bourgalais@univ-lorraine.fr

composed of a hydrogenation Ni bed catalyst, through which a buffer gas and H_2 (also used for the FID) is flowed to reduce species containing carbonyl groups to the corresponding alkanes, and CO and CO_2 to methane. For species identification the GC equipped with a Q-Bond capillary column was coupled to a quadrupole mass spectrometer. Ions were generated via electron impact ionization at 70 eV.

FID and TCD calibrations were performed using gaseous standards provided by Air Liquide for O_2, CH_4, CO, and CO_2. All other species detected with the FID were calibrated using the effective carbon number (ECN) method. Their calibration factors were deduced from those of the calibrated species by taking into account their effective carbon number. The relative uncertainties of the mole fractions of the species calibrated using gaseous standards were estimated to be ±5% while the relative uncertainties of the species calibrated using the ECN method were estimated to be ±10%.

JSR coupled to SVUV-PIMS

The PIMS experimental setup used at the VUV beamline of the NSRL synchrotron has been newly developed at the Atomic & Molecular Physics Beamline (BL09U). A detailed discussion of the experimental setup and the validation of the system will be the subject of a separate publication. Here, only a brief description of the experimental method is given. The design of the JSR is based on the KAUST JSR[30], while the design of the nozzle sampling is similar to that described by Battin-Leclerc et al.[25]. Specifically, a tapered quartz nozzle with a 100 µm orifice is used. The tip of the quartz nozzle is inserted into the JSR to sample the gas and create a molecular beam, which enters the ionization chamber through a skimmer and is crossed by the undulator generated VUV light. The ions resulting from photoionization are then detected with a reflectron time-of-flight mass spectrometer with a mass resolution of ~4,000.

In the experiment, temperature dependence curves of the product's signal are obtained at fixed photon energies, and the species mole fraction can be obtained from the signal. For species *i*, the mole fraction at the different temperatures is calculated with the equation :

$$X_i(T) = X_i(T_0) \times \frac{S_i(T)}{S_i(T_0)} \times \frac{\lambda(T_0)}{\lambda(T)}$$

$X_i(T)$, $\lambda(T)$ and $S_i(T)$ represent, respectively, the mole fraction of species *i* at temperature *T*, the coefficient of gas expansion at temperature *T* depending on the bulk property of the system and the signal of species *i* at temperature *T*. Similarly, $X_i(T_0)$, $\lambda(T_0)$ and $S_i(T_0)$ are known information at temperature T_0, which is usually chosen as the temperature at which no reaction occurs. It is worth noting that the gas expansion factor is obtained through measurements of the change of Ar signal during the experiment.

Species from the low-temperature oxidation experiment of neopentane were ionized at 11.5 eV, 10.5 eV, 9.8 eV and 9.3 eV. An internal standard with a known mole fraction was used at each photon energy to convert the normalized ion signal of a given species to its mole fraction. At the same photon energy, the mole fractions of reaction products can be calculated with the fuel as a reference:

$$X_i(T) = X_{fuel}(T) \times \frac{S_i(T)}{S_{fuel}(T)} \times \frac{\sigma_{fuel}(E)}{\sigma_i(E)} \times \frac{D_{fuel}}{D_i}$$

$\sigma_i(E)$ is the photoionization cross-section of species *i* at the photon energy E. D_i is the mass discrimination factor of species *i*. Neopentane has a very small photoionization cross section (PICS) at the onset of the parent signal at m/z 72 (see Figure 1). Therefore, its daughter ion at m/z 57 was chosen as the internal standard of 11.5 eV. The m/z 57 signal at conditions of no

reaction is used as the signal of internal standards. This ensures that there is no interference from the m/z 57 signal caused by low-temperature reaction products. The PICS of the neopentane daughter ion is very small or zero at 10.5 eV and 9.8 eV. For these ionization energies ketene was chosen as the internal standard. The reason for selecting ketene as the internal standard is that its PICS is available in the literature[31] and its ionization energy is 9.67 eV. For experiments employing 9.3 eV for ionization, 1,3-butadiene was used as the internal standard because its PICS is also available in the literature[31] and its ionization energy is 9.07 eV. The mole fractions of ketene and 1,3-butadiene were in turn quantified at 11.5 eV using m/z 57 as the internal standard. Note that the use of ketene and 1,3-butadiene as internal standard may introduce additional uncertainties of the quantified mole fraction. Result shows that for the intermediates that could be quantified at different energies, mole fractions are in good agreement at the selected energies. The uncertainty in the mole fraction was evaluated to be within ±10% for the reactants, within ±20% for the intermediates with experimentally measured PICS, and estimated to a factor of 2 for the intermediates with calculated PICS. Note that in the rare occasions where experimental and simulated cross-sections are available, larger differences have been reported[32,33].

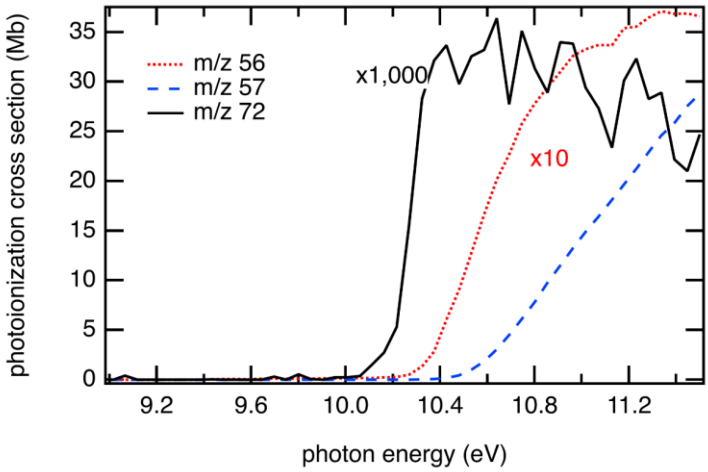

Figure 1. Photoionization cross section of neopentane (solid black line) and its fragments at m/z 56 (dotted red line), and 57 (dashed blue line) from dissociative ionization, recorded at the NSRL.

JSR coupled to SVUV-PEPICO

Inside the SAPHIRS chamber[34] permanent end-station, located at one of the monochromatized branches of the DESIRS beamline at the SOLEIL synchrotron a 100µm sampling nozzle is connected to the JSR, which is operated at a pressure of 1.07bar. The resulting molecular beam passes through two skimmers before entering the ionization chamber where it is crossed by the VUV beam focused at the center of the double-imaging photoelectron/photoion coincidence (i^{2}PEPICO) spectrometer DELICIOUS III. The spectrometer is able to detect electrons and cations in coincidence[35]. Here, this scheme allows the photoelectrons to be filtered by ion mass and ion arrival position, where the latter ensures that only neutrals produced within the reactor are considered, discarding, by ion imaging filtering, the contribution from background gases impinging on a different spatial region of the ion position sensitive detector[36]. The mass spectra obtained with this apparatus have a typical mass resolving power of ~1,700 (FWHM). The photoelectron spectroscopy of

any given mass, a footprint of the electronic structure of the species, can be obtained in the form of a SPES by scanning the photon energy while analyzing the photoelectron energies, using a method previously described[27], with a typical overall resolution of about 20 meV. PIY can also be obtained through integration over all electron energies, even in cases for which the signal-to-background ratio does not allow an electron kinetic energy analysis. Note that time restrictions related to limited synchrotron access prevented the recording of mole fractions at SOLEIL.

The error bars shown in PES are obtained assuming a Poisson distribution on the image pixel counts, which is then propagated throughout all operations using standard formulae. Note that these errors are taken into account when fitting isomer distributions to obtain branching ratios.

Theoretical methods

The equilibrium structures have been determined for neutral and ionic species using the PBE0 density functional[37] as implemented in GAUSSIAN09[38], using the augmented correlation-consistent aug-cc-pVDZ basis set[39,40]. To ensure that the geometries correspond to minima, the conformation space of neutral and cationic species was explored by scanning the dihedral angles responsible for rotor orientation at wB97XD/6-311G(2d,p) level.[41] Zero point vibrational energies (ZPVE) are determined at the anharmonic level as implemented in GAUSSIAN09. A Franck Condon (FC) analysis is performed to simulate the vibrationally resolved electronic spectra at 0 K by means of the Time-Independent Adiabatic Hessian Franck–Condon (TI-AH|FC) model[42–45]. The resulting stick spectrum was convolved with a 20 meV bandwith Gaussian profile to match the experimental resolution.

For the determination of the adiabatic ionization energy (AIE), the CBS-QB3 zero-point vibrational energy (ZPE)-corrected total electronic energies for the neutral and cation ground states have been used in the first place[46,47]. When further clarification was required, the geometry optimizations were followed by single point computations on the optimized structures using the explicitly correlated coupled cluster with single, double and perturbative triple excitations ((R)CCSD(T)-F12)[48–51] together with the aug-cc-pVDZ basis set in conjunction with the corresponding resolutions of the identity and density fitting functions[52] as generated by MOLPRO[53]. Afterwards, the computed spectra at the PBE0/aug-cc-pVDZ(opt)//(R)CCSD(T)-F12/aug-cc-pVDZ(SP) level were shifted in energy so that it best matches the experimental spectra. When available, comparison between experimental reference spectra and the simulated spectra is presented to provide a benchmark of the theoretical methodology. Note that only the most stable conformer of each isomer at a given m/z has been taken into account to simulate the spectrum.

Kinetic model

The experimental mole fractions measured during the oxidation of neopentane were compared to numerical predictions with the detailed kinetic model of pentane isomers developed at NUI Galway[11]. This model was used without any modifications. It predicts the auto-ignition delay times of pentane isomers measured in a rapid compression machine and a shock tube well[11], and it was also previously used to reproduce experimental oxidation data of n-pentane obtained in JSRs at 1 and 10 bar[54]. All simulations described in this work were performed using the openSMOKE++ software package[55,56].

*corresponding author: jeremy.bourgalais@univ-lorraine.fr

Results and Discussion

Neopentane conversion

In all figures, expect for SPES, the mole fractions represented by blue circles were obtained by GC analysis at LRGP and green triangles by PIMS at NSRL. The red line correspond to numerical simulations. Figure 2 presents the conversion of neopentane measured at $\phi = 0.5$ and the temperature range T = 500 – 850 K, and it compares the experimental data with predictions by the kinetic model. It should be noted that neopentane oxidation was studied for temperatures up to 1,100 K. However, oscillatory behaviors was observed at temperatures above 1,000 K. This transient evolution of the mole fractions of reactants and products during oscillating limited cycles have already been observed in the literature during fuel combustion at high temperatures[57–59]. As oscillatory chemistry is not the subject of this work only data up to 850 K are considered.

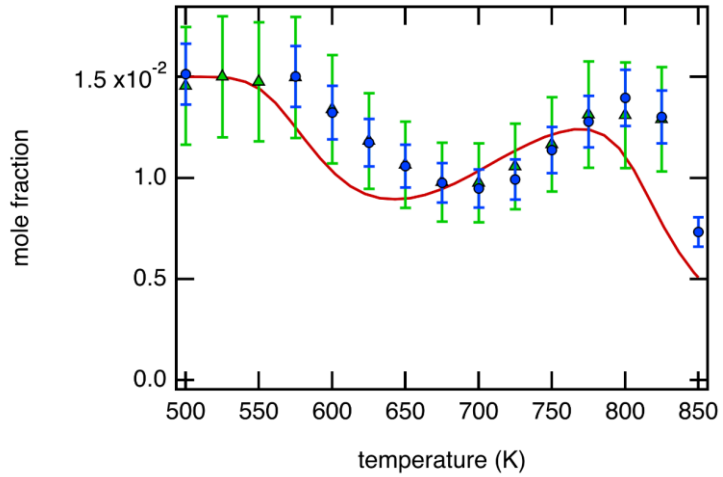

Figure 2. Fuel conversion during neopentane JSR oxidation between experimental measurements (GC and PIMS) and numerical predictions (neopentane 1.5 %, $\phi = 0.5$, $\tau = 3$ s).

In Figure 2, the experimental data for the conversion of neopentane show a notable low temperature reactivity and a marked negative temperature (NTC) zone which are reproduced by the kinetic model. The degree of conversion and the width of the NTC region are well captured by the kinetic model. However, in the model prediction the fuel conversion starts at a temperature ~60 K lower than observed in the NSRL and LRGP experiments. The good agreement between both experimental measurements (GC and PIMS) suggests that the fuel reactivity is overestimated by the kinetic model and that the initiation chemistry need to be revised. The overprediction of the neopentane reactivity by the kinetic model was also observed in the experimental conditions used by Hansen et al.[20] (see SM of this paper). Note that the same JSR has been used at SOLEIL and LRGP, while the NSRL JSR has a different design but both of them have been used for numerous oxidation studies in the past and temperature shifts were never observed.

At LRGP, the mole fraction of neopentane is proportional to the FID signal measured after GC separation, of the species contained in the effluent gas mixture. In contrast, as mentioned in the experimental methods section, at NSRL the quantification was done indirectly through the dissociative ionization fragment of neopentane at m/z 57 ($C_4H_9^+$), which has a much higher photoionization cross section than the parent ion (see Figure 1). The

*corresponding author: jeremy.bourgalais@univ-lorraine.fr

observed good agreement demonstrates the reliability of this indirect quantification procedure when the photoionization cross section is known.

The dissociation of the neopentane cation to m/z 56 (CH_4 loss) and 57 (CH_3 loss) fragment ions has been recorded without O_2 addition using the i^{2}PEPICO spectrometer, in order to deconvolve the fuel contribution to these mass channels in oxidation conditions from contributions by product species. The mass-selected normalized SPES of the parent and the fragments are shown in the left panel of Figure 3. They agree with the previously reported breakdown diagram and appearance energies[60]. Figure 3 (right panel) shows the total SPES associated to neopentane, i.e. summing the non-normalized signals from m/z 72, 56, and 57. As a benchmark of the theoretical methodology, the PES for electronic ground state neopentane ionization was simulated. The simulated PES shows a broad and unstructured vibrational envelop due to the geometry changes upon ionization caused by the Jahn-Teller distortion[61], in good agreement with the experimental data. An AIE = 10.05 eV is obtained from matching the calculated and experimental envelops, 160 meV lower than existing values[62].

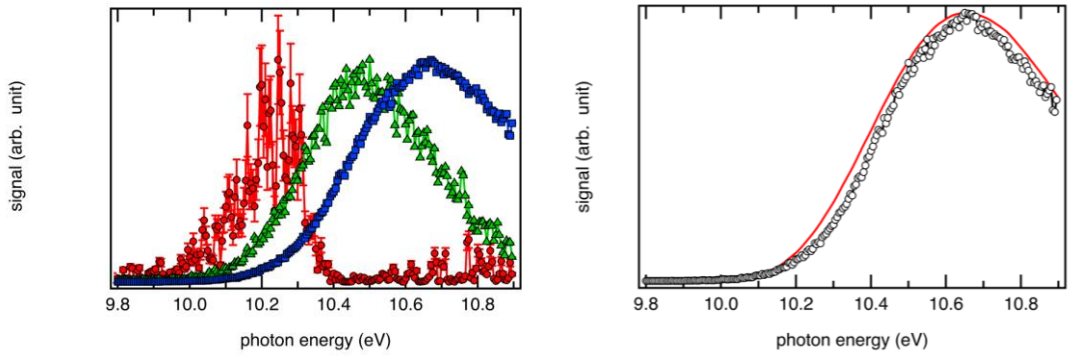

Figure 3. (left) Normalized SPES of m/z 56 (green triangles), 57 (blue squares), and 72 (red dots) obtained at SOLEIL in experiments in which neat neopentane is flowed through the JSR at 580 K. (right) Sum of non-normalized SPES of m/z 56, 57, and 72 (dots) compared to simulated PES of neopentane (red line). The simulated PES has been shifted by 77 meV to match the experimental curve.

Products from the first O_2-addition

Figure 4 reports a rate of production analysis carried out at 600 K for JSR experiments at ϕ = 0.5 using the kinetic model by Bugler et al.[11]. Based on the literature[17], the low-temperature oxidation of neopentane is controlled by the formation of a neopentyl radical (R) that further reacts with O_2 to form a neopentylperoxy radical (ROO). The predicted dominant fate of the ROO radical is isomerization to give the hydroperoxyneopentyl radical (QOOH) via a cyclic 6-membered transition state. According to the model, at 600 K, 31% of hydroperoxyneopentyl converts to 3,3-dimethyloxetane (CC1(COC1)C, m/z 86) through ring-closure of the hydroperoxy neopentyl radical and simultaneous OH elimination.

*corresponding author: jeremy.bourgalais@univ-lorraine.fr

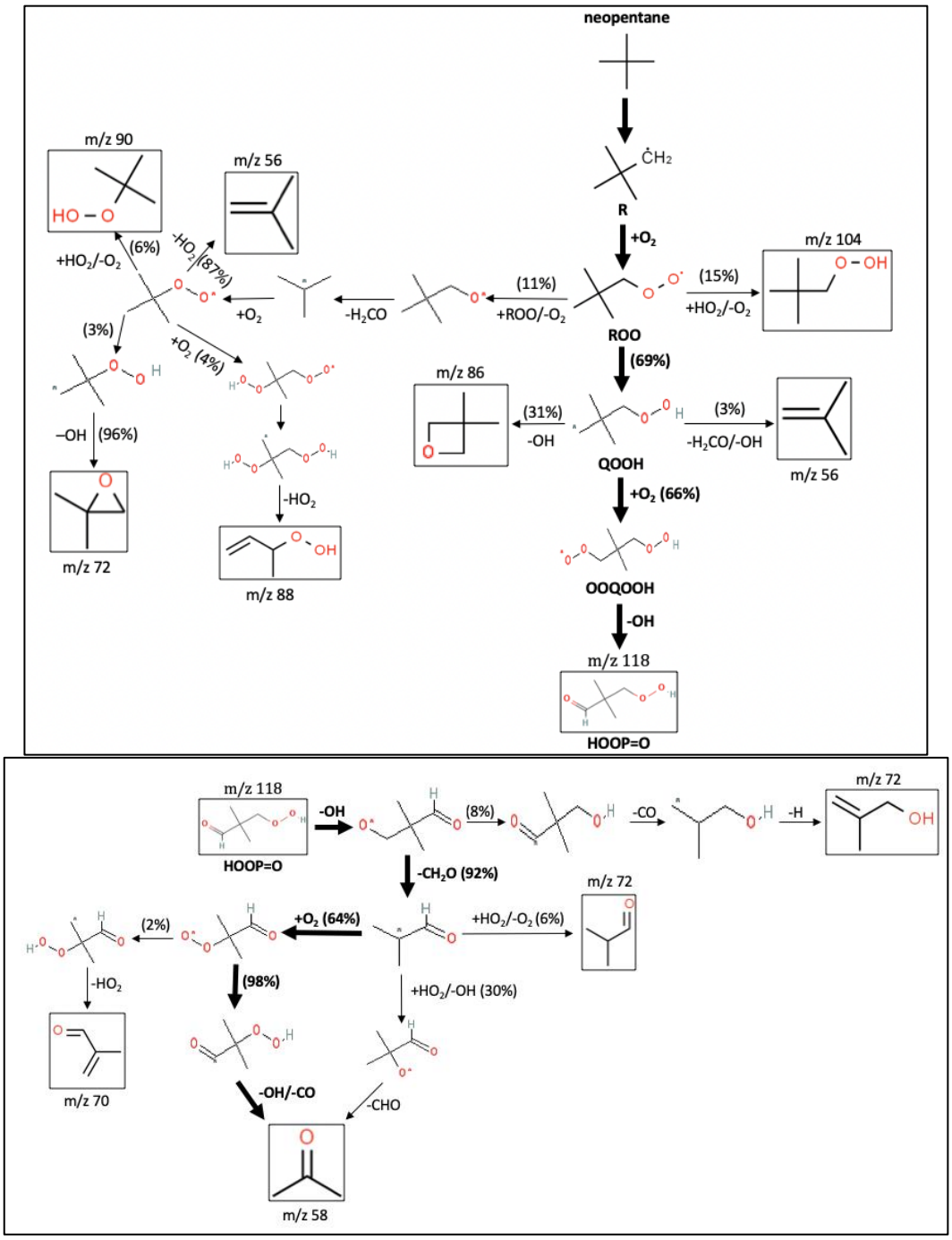

Figure 4. Rate of production analysis for neopentane oxidation (ϕ = 0.5, 1.5 % in He) at 600 K, P = 1.07 bar and τ = 3 s. Bold arrows indicate the dominant pathways. Pathways with small branching ratios (< 1 %) to or from intermediates are omitted for clarity. The upper panel shows the reactions leading to the formation of KHP. The lower panel shows the decomposition pathways of KHP.

The right panel in Figure 5 compares the SPES of m/z 86 recorded at 580 K compared to simulated SPES of 3,3-dimethyloxetane and three isomers: 2,2-dimethylpropanal CC(C)(C)C=O, trans-2,4-dimethyloxetane CC1CC(O1)C, and pentan-3-one CCC(=O)CC. The deconvolution of the SPES leads to a 3,3-dimethyloxetane:2,2-dimethylpropanal:trans-2,4-dimethyloxetane:pentan-3-one signal branching ratio of 0.5:1.0:0.1:0.3. 3,3-dimethyloxetane and 2,2-dimethylpropanal spectra have their bands overlapping, but the SPES is found to be

mostly similar to that of 2,2-dimethylpropanal. A small contribution is also found from trans-2,4-dimethyloxetane and pentan-3-one but the congestion of the spectra in such out of equilibrium environment make the conclusion to be taken with care. The photoionization cross section of 2,2-dimethylpropanal could not be found in the literature making it impossible, at this time, to validate the calculations through experimental branching ratios. 2,2-dimethylpropanal is known to fragment to m/z 57 ($C_3H_5O^+$) with an AIE = 9.51 eV[63]. The observed increase in the SPES signal of m/z 57 under oxidizing conditions in the region, in which the 2,2-dimethylpropanal fragment is expected, supports the formation of 2,2-dimethylpropanal (see Figure S1).

The left panel in Figure 5 shows the recorded mole fraction profiles of 3,3-dimethyloxetane using either GC or PIMS detection and quantification. Taking into account an uncertainty estimated to be ±50% for 3,3-dimethyloxetane in PIMS measurements, the GC and PIMS data agree well. In the PIMS experiments, 3,3-dimethyloxetane has been quantified using the ion fragment (m/z 56) at 9.8 eV. This required the contribution of isobutene to be subtracted from the signal of m/z 56, which explains the rather high uncertainty of the 3,3-dimethyoxetane mole fractions.

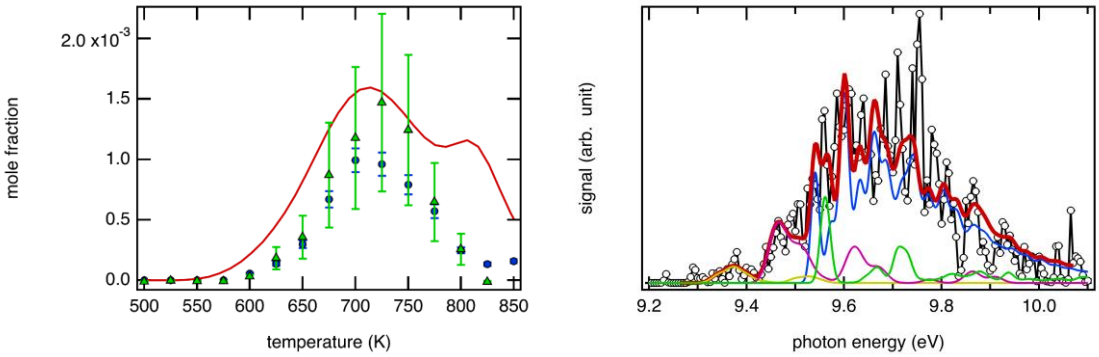

Figure 5. (left) Mole fraction profile of 3,3-dimethyloxetane measured during neopentane oxidation (ϕ = 0.5, 1.5 % in He) at P = 1.07 bar and τ = 3 s. **The model prediction is also presented. (right) SPES of m/z 86 at 580 K (dots) compared to simulated spectra of trans-2,4-dimethyloxetane (yellow line), pentan-3-one (purple line), 3,3-dimethyloxetane (green line), and 2,2-dimethylpropanal (blue line).** The red line shows the results of the fit (see text for details).

Note that at 600 K very little 3,3-dimethyloxetane is detected. The GC yields at LRGP are only slightly outside of the noise level and the yields determined by PIMS are essentially around zero level. The kinetic model predicts higher yields because of the temperature shift. Taking the shift into account, at best a very small amount of 3,3-dimethyloxetane is predicted at this temperature. Overall, the kinetic model satisfactorily reproduces the 3,3-dimethyloxetane mole fraction profile (shape) and peak value, except for the highest temperatures at which 3,3-dimethyloxetane is overpredicted.

In the study by Eskola et al.[17], 3,3-dimethyloxetane was shown to hardly produces a signal at m/z 86 but instead fragments to m/z 56. The signal of the fragment is more than 1,000 times stronger than that of the parent ion. If the 2,2-dimethylpropanal cation does not significantly fragment, then it is clear that essentially all signal at m/z 86 arises from 2,2-dimethylpropanal, in agreement with the analysis presented above. Eskola et al.[17] also determined relative yields for 3,3-dimethyloxetane and 2,2-dimethylpropanal for three temperatures: 575 K, 625 K, and 675 K. They found the 2,2-dimethylpropanal yield to decline

with increasing temperature while the highest 3,3-dimethyloxetane yield relative to isobutene was found at 625 K. From their data, the 3,3-dimethyloxetane:2,2-dimethylpropanal ratios for the three temperatures are 2.8, 10.1 and 21.3. Since the PIMS and GC measured mole fractions are already at the detection limit for 3,3-dimethyloxetane at temperatures below 600 K, this explains why 2,2-dimethylpropanal was not detected with these devices at low temperatures.

At higher temperatures, the 2,2-dimethylpropanal concentration should reach around 100 ppm if the relative yields reported by Eskola et al.[17] for Cl initiated oxidation are applicable to the thermal oxidation of neopentane under the conditions of this study. This is not guaranteed since Eskola et al.[17] speculate that 2,2-dimethylpropanal "could originate at least partly from radical-radical reactions" and the radical concentrations in their work likely differ substantially from those in the JSR experiments reported here. In any case, the expected yields of 2,2-dimethylpropanal compared to 3,3-dimethyloxetane are so low that any missing signal of 2,2-dimethylpropanal has no notable impact on the mass balance or total ion counts in the PIMS experiment. Future SPES measurements (m/z 86 and 56) as a function of temperature would be helpful to verify the branching ratio reported by Eskola et al.[17]. Any further attempts to search for 2,2-dimethylpropanal should focus on the temperature range above 625 K.

Although the formation of 2,2-dimethylpropanal is not predicted by the kinetic model, the work by Eskola et al.[17] as well as this study has clearly proven its presence. Besides the possibility to be formed in radical-radical reactions (Eskola et al.[17]), another reaction sequence could be a successive migration of two H atoms starting from the ROO radical, followed by the removal of an OH group:

$$C_3CCOO^{\cdot} \rightarrow C_2C(C^{\cdot})COOH \rightarrow [C_3CC^{\cdot}OOH] \rightarrow C_3CCHO + OH$$

This sequence may be competitive to the oxetane formation channel and should be investigated to ensure that all 2,2-dimethylpropanal related chemistry is properly included in the kinetic model.

Eskola et al.[17] recorded the photoionization signal at m/z 56 to address the formation of 3,3-dimethyloxetane. The signal at m/z 56 is a combination of signals originated from isobutene (C_4H_8) and fragments from dissociative ionization of 3,3-dimethyloxetane (m/z 86) and neopentane (m/z 72). The right panel of Figure 6 compares the difference between SPES of m/z 56 at 580 K with and without O_2 addition to a reference PES of isobutene. The low photon energy region overlaps with the isobutene reference PES while above 10.5 eV, according to the results of Eskola et al.[17], the spectral signature arises from the fragmentation of 3,3-dimethyloxetane.

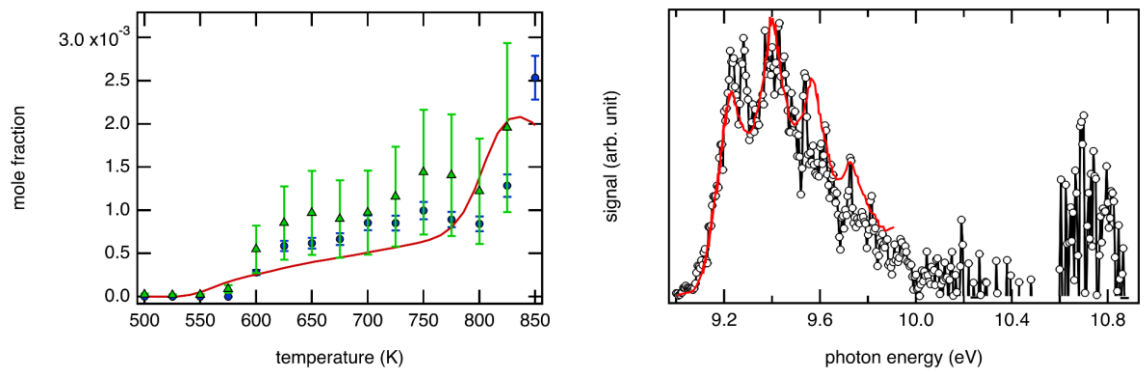

Figure 6. (left) Mole fraction profile of isobutene measured during neopentane oxidation (ϕ = 0.5, 1.5 % in He) at P = 1.07 bar and τ = 3 s. The model prediction is also presented. (right)

Difference between SPES of m/z 56 at 580 K with and without O_2 addition (dots). The PES of isobutene (red line) from Mintz & Kuppermann[64], scaled to match the peak, is shown too.

Isobutene is formed in a pathway competing with 3,3-dimethyloxetane formation during the QOOH radical decomposition (see Figure 4). The left panel in Figure 6 shows good agreement between simulated and experimental isobutene mole fractions obtained at LRGP when the 60 K shift is taken into account. In order to eliminate the interference of 3,3-dimethyloxetane ion fragment (m/z 56), the mole fraction of isobutene has been determined in the PIMS experiments at 9.3 eV. As mentioned above, 1,3-butadiene was used as the internal standard to quantity the mole fraction of isobutene and the uncertainty of the isobutene mole fraction is estimated to be ±50%. Taking the uncertainties into account, PIMS and GC data are in good agreement. The more straightforward GC quantification makes this data more reliable, though. Isobutene formation from QOOH releases an OH radical and formaldehyde (CH_2O, m/z 30) as by-products but the modeled profiles of isobutene and CH_2O are clearly different, suggesting that CH_2O is mainly produced by a different channel.

CH_2O was detected in the GC, PIMS, and PEPICO experiments (see Figure 7). While PIMS derived mole fractions are in relatively satisfactory agreement with numerical predictions, again if one accounts for 60 K shift in neopentane conversion, the concentrations measured by GC and PIMS differ by as much as a factor of 40 as highlighted in the left panel of Figure 7, even though the overall shapes are in agreement. At the highest temperatures reached in this work, the model overpredicts CH_2O but the shape follows that of the experimental trends.

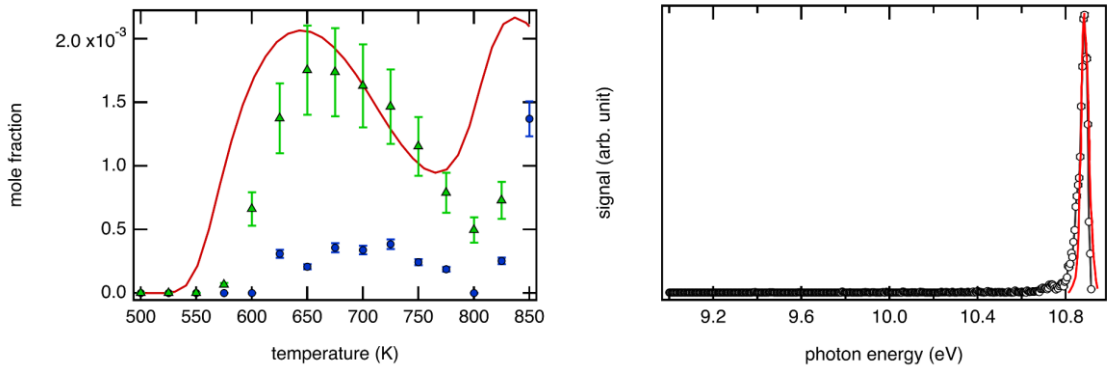

Figure 7. (left) Mole fraction profile of CH_2O measured during neopentane oxidation (ϕ = 0.5, 1.5 % in He) at P = 1.07 bar and τ = 3 s. GC mole fractions (blue dots) have been multiplied by 10. The model prediction is also presented. (right) SPES of m/z 30 at 580 K (dots) compared to the PES of CH_2O (red line) from Baker et al.[65].

Formaldehyde is one most important intermediate in low-temperature oxidation, thus PIMS mole fractions at a level of 10^{-3} seems thus reasonable. Note that, because of the larger deviation with GC data for this species, in order to verify the reliability and rationality of experimental results for neopentane, experiments have been repeated also in the Combustion and Flame Beamline (BL03U) of NSRL. The JSR used at BL03U is the same as the one used in LRGP. Good agreement with the data obtained at BL09U is observed for the species presented, so that the PIMS experimental methodology is considered reliable. In the meantime, to ensure the reliability of the measurements obtained by GC, GC measurements have been also repeated at the same conditions with the unaltered setup but a different

operator. The mole fraction results were very close to the original data, with relative deviations of less than 2%. However, the unexpected large presence of formic acid (see further more explanation below) might cause polymerization problems of CH_2O in the GC transfer lines.

The disagreement of the formaldehyde data – although unfortunate – show the value of collaborations with complementary independent detection systems. Without these redundant data sets, there would have been no incentive to double-check the results as the good reproducibility of the individual measurements obscures the existence of a problem. Further studies are necessary to confirm our current interpretation that the PIMS data are correct and the GC data suffer from formaldehyde polymerization issues.

KHP formation from the second O_2-addition

The second addition of O_2 leads to the formation of a hydroperoxyalkylperoxy radical (OOQOOH), especially at high pressures and high O_2 mole fractions, such as in practical combustion systems. This radical subsequently decomposes to 3-hydroperoxy-2,2-dimethylpropanal CC(C)(COO)C=O, a KHP, and an OH radical. The KHP was detected directly at m/z 118 in the NRSL experiments and the signal profile at ϕ = 0.5 is displayed in the left panel of Figure 8 along with the predicted mole fractions . Both profiles are in relatively good agreement (shape and position) if the systematic shift of the predictions by 60 K is taken into account. The mole fraction profile peaks over a small temperature range centered at 600 K, which is in good agreement with the measured 590 K maximum at ϕ = 0.9 in Hansen et al.[20].

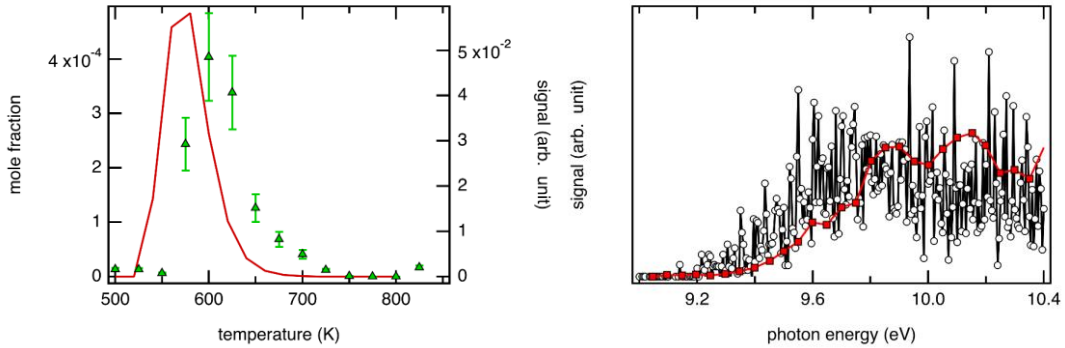

Figure 8. (left) Simulated mole fraction profile of γ-KHP compared to signal of m/z 118 measured in PIMS during neopentane oxidation (ϕ = 0.5, 1.5 % in He) at P = 1.07 bar and τ = 3 s. (right) PIY of m/z 90 at 580 K (black dots) compared to a PIY curve of m/z 90 from Hansen et al.[20] (red line).

The formation of KHP could not be observed directly at m/z 118 of the parent ion in the SOLEIL experiments (see Figure 9 for typical mass spectra obtained during SOLEIL and NSRL experiments). This was due to an insufficient signal to noise ratio in the SOLEIL setup, which might be caused by the relatively long (14 cm) distance between the nozzle tip to the point of ionization. The density in a molecular beam decreases quasi-linearly with distance. Even though similar gas mixtures were used, a straightforward interpretation of the differences between mass spectra is difficult because, among other reasons, the mass spectra were recorded at different temperatures and the extraction electric fields used in the both setups differed. The detection of KHPs at m/z 118 is also complicated by fragmentation of the parent ion upon photoionization. Hansen et al.[20] mentioned that the first fragment of KHPs is formed at a photon energy in the range 9.3 - 9.5 eV leading to the $HOOCH_2C(CH_3)_2H^+$ daughter ion at

m/z 90. A signal at m/z 90 was observed with the SOLEIL device and the PIY is displayed in the right panel of Figure 8. The derived appearance energy of 9.2 eV is in relatively good agreement with that mentioned by Hansen et al.[20]

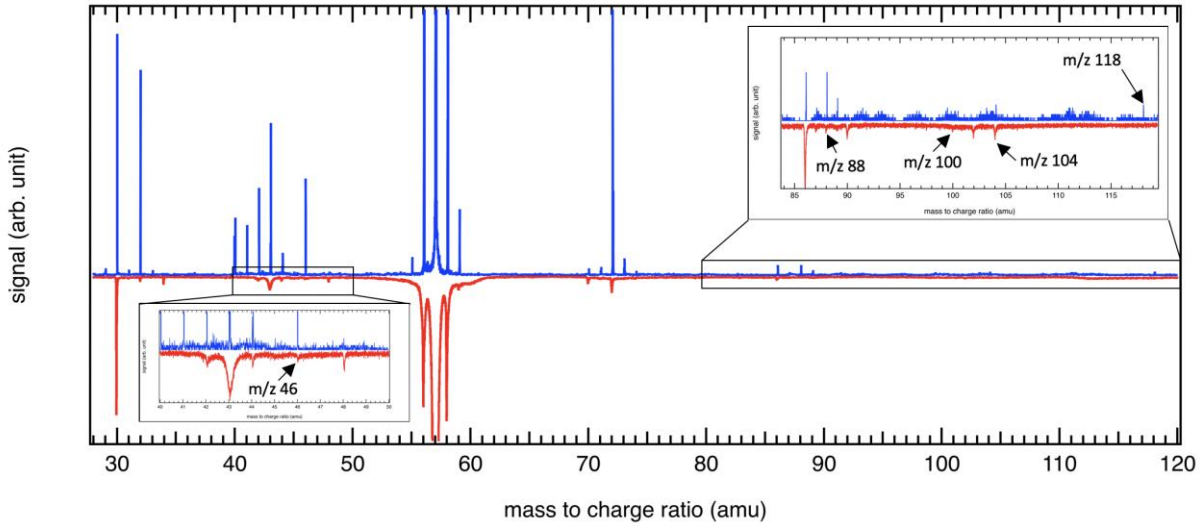

Figure 9. Typical mass spectra: NSRL at 575 K (blue line) and SOLEIL at 600 K (red line) for a photon energy of 11.5 eV and ϕ = 0.5 during the low temperature oxidation of neopentane.

Products from KHP decomposition

Once formed, KHPs decompose through dissociation pathways that remain to be clarified. Eskola et al.[17] observed a peak at m/z 100 which can be attributed to 2,2-dimethylpropanedial CC(C)(C=O)C=O. They hypothesized that it could be formed directly by elimination of a water molecule from KHP. No dialdehyde was detected by GC analysis, but a weak signal at m/z 100 was detected in both, the experiments at SOLEIL and at NSRL experiments (see Figure 9). The signal-to-noise ratio was too low in the PEPICO experiments to measure a sufficiently resolved signal, but the PIY of NSRL fits reasonably well with the simulated PIY of 2,2-dimethylpropanedial (see right panel in Figure 10). The ionization threshold is in good agreement with the AIE = 9.39 eV calculated in Eskola et al.[17] at the CBS-QB3 level of theory. These agreements would support assignment of the m/z 100 signal to 2,2-dimethylpropanedial but new experiments with a better signal to noise ratio are necessary to record an experimental photoelectron spectrum and to compare it with the theoretical one. The signal of m/z 100 as a function of temperature is displayed in the left panel in Figure 10. The maximum of the mole fraction is reached above 700 K. This temperature is rather high for the m/z species to be formed from a KHP since KHP's start to decompose at significantly lower temperatures (see Figure 8). The kinetic model does not contain 2,2-dimethylpropanedial chemistry and thus cannot support the assignment of the data. If the formation of 2,2-dimethylpropanedial were confirmed experimentally, then the neopentane oxidation model would be incomplete and would require an upgrade. Possible missing reactions could be of the type KHP + CH_3 → $C_2C(COOH)C^{\cdot}=O$ + CH_4 and KHP + CH_3 → $C_2C(CHO)_2$ + OH + CH_4.

*corresponding author: jeremy.bourgalais@univ-lorraine.fr

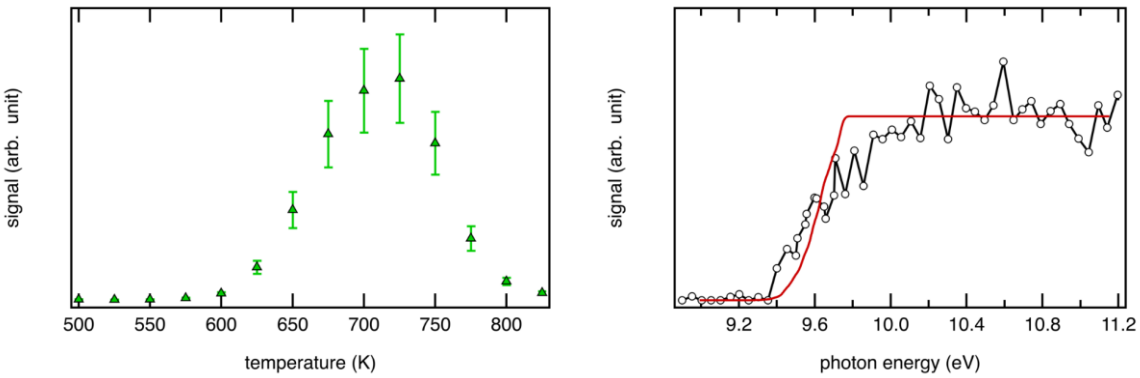

Figure 10. (left) PIMS signal profile of m/z 100 during neopentane oxidation (ϕ = 0.5, 1.5 % in He) at P = 1.07 bar and τ = 3 s. (right) PIY of m/z 100 derived from NSRL (dots) to simulated PIY of 2,2-dimethylpropanedial (red line).

KHPs (HOOP=O) mainly decompose via -O-OH bond rupture, which leads to chain-branching due to the reactivity of the O-centered isobutanal-2-methyloxy radical (OPO). Subsequent reactions form species with atomic masses of 58, 70, and 72 (see Figure 4). The dominant decomposition pathways consist of CH_2O-loss, mainly leading to acetone (m/z 58). The acetone profiles measured by NSRL and LRGP agree reasonably well given the uncertainties of the calibrations (see left panel in Figure 11). Good agreement is also found between predicted and experimental mole fractions of acetone. The SPES of m/z 58 (see right panel in Figure 11) confirms the assignment of the spectral features to the acetone cation, in agreement with the results from Eskola et al.[17] Consequently, other potential isomers (propanal, methyloxirane) can be safely be ruled out.

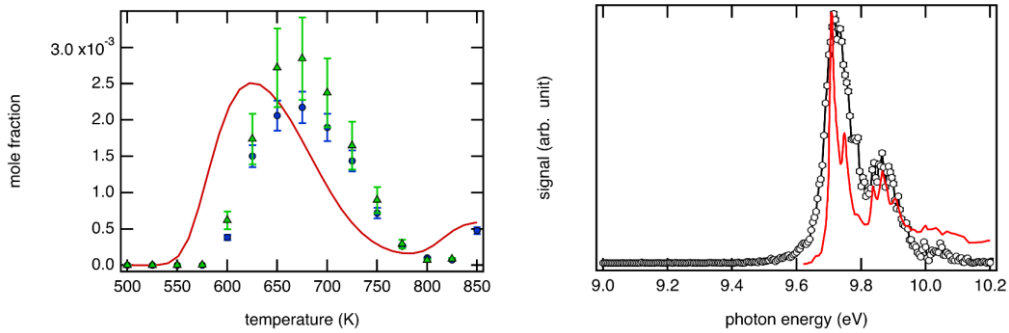

Figure 11. (left) Mole fraction of acetone measured during neopentane oxidation (ϕ = 0.5, 1.5 % in He) at P = 1.07 bar and τ = 3 s. The model prediction is also presented. (right) SPES of m/z 58 at 580 K (dots) compared to TPES of acetone (red line) from Rennie et al.[67].

According to the kinetic model, a minor decomposition pathway of the KHP leads to methacrolein (CC(=C)C=O, m/z 70). The left panel in Figure 12 shows that the simulation predicts for the central temperature regime studied lower methacrolein mole fractions than measured in both setups. At 700 K, at which the methacrolein mole fraction peaks, the deviation is about a factor of two. The agreement between PIMS and GC is good considering that the PICS of 2-butenal has been used to estimate the PICS of methacrolein. The PICS of 2-butenal is generally considered to have an uncertainty factor of 2. The SPES of m/z 70 is displayed in the right panel of Figure 12 and the simulated PES of methacrolein matches the first band fits rather well with the simulated PES of methacrolein. The AIE calculated in this

work is 9.91 eV which is in very good agreement with the experimental AIE of 9.92 eV reported in the literature[66]. The contribution of other potential isomers (1,1-dimethyl cyclopropane CC1(CC1)C, methyl vinyl ketone CC(=O)C=C) can be safely ruled out based on their simulated or experimental photoelectron spectra.

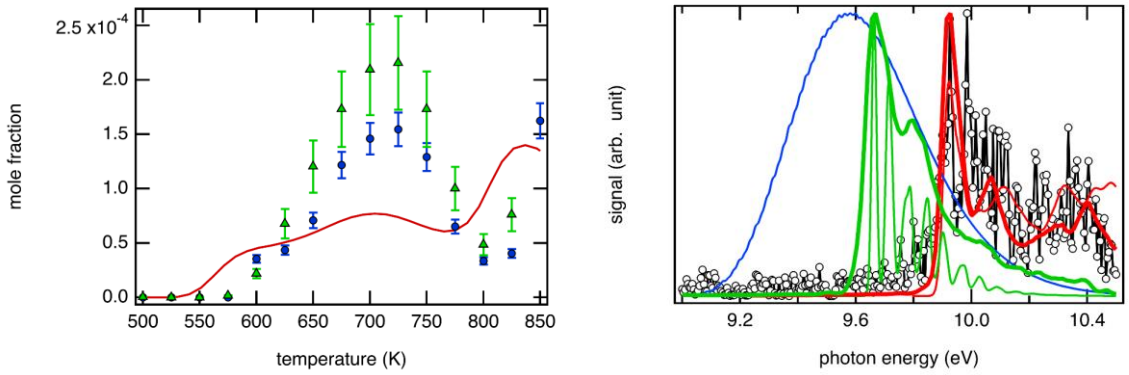

Figure 12. (left) mole fraction of methacrolein measured during neopentane oxidation (ϕ = 0.5, 1.5 % in He) at P = 1.07 bar and τ = 3 s. The model prediction is also presented. (right) SPES of m/z 70 at 580 K (dots) compared to simulated PES of methacrolein (red line), methyl vinyl ketone (green line), and 1,1-dimethyl cyclopropane (blue line). Reference experimental PES of methyl vinyl ketone (bold green line) and methacrolein (bold red line) recorded at low resolution and at photon energy of 10.4 eV with the PEPICO facility are also plotted as a gauge of the simulation quality.

Reported in Figure 4, another minor pathway involving the loss of CH_2O and a successive HO_2-addition/O_2-elimination leads to 2-methylpropanal (CC(C)C=O, m/z 72). The left panel of Figure 13 shows a reasonably good agreement between the numerical and LRGP experimental mole fractions, except at 600 K where the discrepancy is significant (almost an order of magnitude difference). The PIMS data shown in Figure 13 are significantly higher than the GC measurements. This is likely due to contribution of additional species, such as 2,2-dimethyloxirane, to the m/z 72 signal. This explanation is supported by the right panel of Figure 13 which clearly shows that the m/z 72 spectrum cannot be reproduced by 2-methylpropanal alone. See also the next section for further explanations. Eskola et al.[17] proposed a parallel decomposition pathway for KHP via intermediate cyclic peroxide formation rather than direct OH-loss. This mechanism, called Korcek reaction, is known to lead through subsequent decomposition to a carbonyl compound and an organic acid[23]. In the case of neopentane, the Korcek reaction of its KHP produces 2-methylpropanal as carbonyl component accompanied by formic acid (HCOOH, m/z 46) (see Figure 14). The maximum deviation between numerical and experimental mole fractions of 2-methylpropanal coincides with the maximum mole fraction of KHP (600 K, see Figure 8), which supports the idea that the missing Korcek reaction in the model causes the discrepancy between experiment and model.

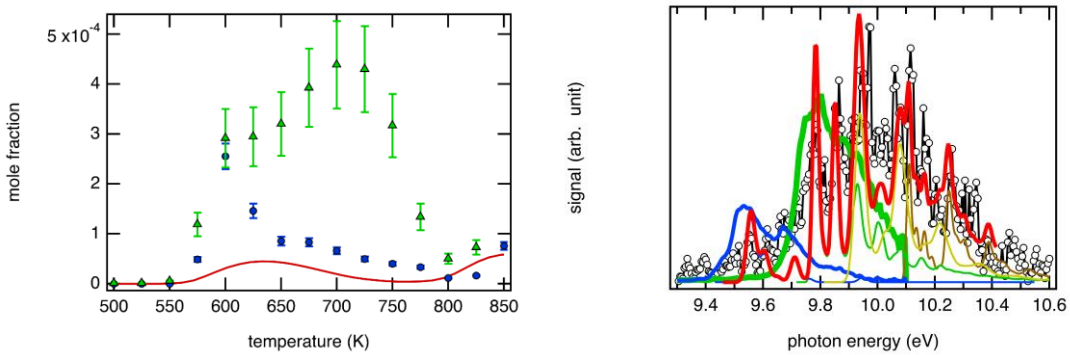

Figure 13. (left) Mole fraction of 2-methylpropanal measured by GC and m/z 72 measured by PIMS during neopentane oxidation (ϕ = 0.5, 1.5 % in He) at P = 1.07 bar and τ = 3 s compared to literature model predictions. (right) SPES of m/z 72 at 580 K (dots) compared to simulated spectra of butan-2-one (blue line), 2-methylpropanal (green line), trans-2,3-dimethyloxirane (yellow line), and 2,2-dimethyloxirane (brown line). Reference experimental PES of butan-2-one (bold blue line) and 2-methylpropanal (bold green line) from Pieper et al.[68] are also plotted as a gauge of the simulation quality. The bold red line shows the results of the fit (see text for details).

In agreement with this Korcek-type pathway interpretation, a signal at m/z 46 was recorded in the NSRL experiments (see NSRL mass spectrum reported in Figure 9). A signal at m/z 46 was also observed in a SOLEIL mass spectrum recorded at 11.5 eV (see the insert in Figure 9) supporting the formation of formic acid (AIE = 11.31 eV)[63]. A SPES is not available since the AIE falls outside the energy range of the scans performed at SOLEIL. However, the PIY measured in PIMS experiments shown in the left panel of Figure 15 fits well with a reference PIY of formic acid from Battin-Leclerc et al.[29]. Note that the FID detector is usually not sensitive to formic acid, which makes it difficult to identify this species in GC experiments. The observed formation of formic acid is in agreement with the higher pressure work of Wang et al.[14] at ϕ=0.3, who measured experimentally a significant mole fraction of HCOOH with a maximum yield at 645 K. Their model does not predict any reaction until the temperature reaches 630 K and Wang et al.[14] introduced a HCOOH production pathway from CH_2O but mentioned the possibility of another unknown formation pathway. This pathway could be related to the Korcek reaction, which is not included in the current kinetic model (see Figure 4) and would provide a plausible explanation for the underestimation of 2-methylpropanal (see left panel in Figure 13) and the detection of HCOOH. It would also provide a parallel decomposition mechanism for KHP in competition with the OH-elimination channel. It means that if KHP were consumed by the Korcek pathway, less CH_2O would be produced (see Figure 4) and the predicted CH_2O yields would be lower. Because the Korcek reaction competes with OH forming reactions, it should reduce the reactivity at low temperatures through the formation of closed-shell species. Therefore, this reaction should be included in an updated neopentane low temperature oxidation model.

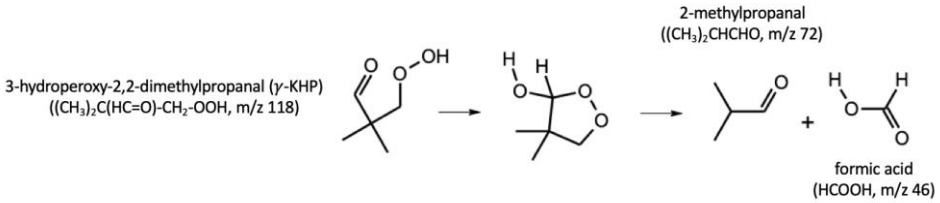

Figure 14. Potential Korcek reaction from γKHP leading to 2-methylpropanal and formic acid.

A weak signal was detected for m/z 88 in both, PIMS and PEPICO experiments but the signal-to-noise ratio was too low in the PEPICO measurements to get a sufficiently resolved signal. The PIMS PIY of m/z 88 is displayed in the right panel of Figure 15. The PIMS PIY is compared to a reference PIY of isobutyric acid ($(CH_3)_2CHCOOH$)[69] and simulated spectra of two isomers 3-hydroperoxybut-1-ene CC(C=C)OO and 3-hydroperoxy-2-methylprop-1-ene CC(=C)COO. The reference spectrum of isobutyric acid does not seem to correspond to the PIMS PIY. Furthermore, even though the ionization threshold is difficult to distinguish (between 9.8 and 10.2 eV) because of the low signal to noise ratio, it seems to be slightly lower than that of isobutyric acid. Moreover, the spectrum of isobutyric acid does not have a plateau as pronounced as in the PIMS PIY and increases from 11.4 eV, which does not seem to be the case for the PIMS PIY. Another possibility is that the observed signal at m/z = 88 corresponds to 3-hydroperoxy-2-methylprop-1-ene, which can be formed by a termination reaction between the allylic isobutenyl radical and HO_2. This reaction is now routinely incorporated in the alkene submechanisms[70], and the resulting hydroperoxide can then yield the conjugated unsaturated aldehyde (in this case, methacrolein). This would be consistent with the high mole fractions of isobutene and methacrolein observed. The calculated AIE is 9.45 eV at the CBS-QB3 level. However, the PIMS PIY better matches the simulated spectrum of 3-hydroperoxybut-1-ene (see right panel in Figure 15). The AIE is calculated to be 9.38 eV at the CBS-QB3 level. 3-hydroperoxybut-1-ene is predicted by the kinetic model as a product in the sequence of reactions initiated by the ROO + ROO reaction (see Figure 4).

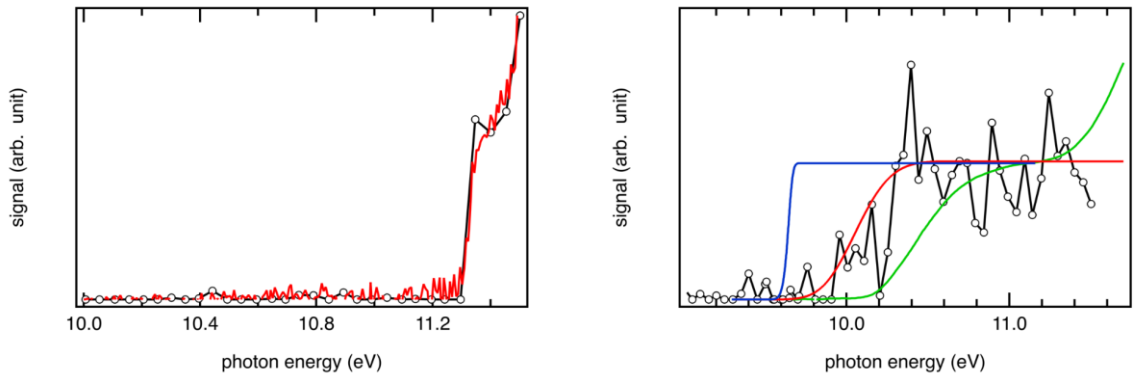

Figure 15. (left) PIY of m/z 46 registered in PIMS measurements at 600 K (dots) compared to a reference PIY of formic acid from Battin-Leclerc et al.[29] (red line). (right) PIY of m/z 88 registered in PIMS at 600 K (dots) compared to a reference PIY of isobutyric acid from Watanabe et al.[69] (green line) and simulated PIY of 3-hydroperoxybut-1-ene (red line) and 3-hydroperoxy-2-methylprop-1-ene (blue line). Note that the PIY of 3-hydroperoxybut-1-ene has been shifted by 100 meV.

New experiments over a wider energy range and leading to better signal to noise detection of m/z 88 would be necessary to confirm this result. Based on the currently available data, m/z 88 does not appear to correspond to isobutyric acid but rather to 3-hydroperoxybut-1-ene. The identification of isobutyric acid next to formic acid, and 2-methylpropanal would have been an additional argument for the Korcek reaction to play a role in the neopentane oxidation, because a second decomposition pathway of the Korcek reaction may lead to the formation of isobutyric acid and CH_2O. However, 3-hydroperoxybut-1-ene is also a reasonable species as it is predicted by the kinetic model as a product in the sequence of reactions initiated by the ROO + ROO reaction.

Side products from neopentane oxidation

In the right panel of Figure 13, the SPES deconvolution of m/z 72 using simulated spectra gives a butan-2-one:2-methylpropanal:trans-2,3-dimethyloxirane:2,2-dimethyloxirane signal branching ratio of 0.3:1.0:0.7:0.5. Besides the dominant contribution of 2-methylpropanal, the signature of two oxirane isomers (2,2-dimethyloxirane CC1(CO1)C and trans-2,3-dimethyloxirane CC1C(O1)C) and butan-2-one CCC(=O)C fits with the ones of the SPES. From the kinetic model simulations obtained at the relatively low temperature of 600 K, 2,2-dimethyloxirane results from the direct addition of HO_2 to isobutene[15] and a sequence of reactions initiated by the ROO + ROO. As the temperature increases, the unimolecular decomposition of the radical R to isobutene + CH_3 will counterbalance the reaction R + O_2 → RO_2. The kinetic model also predicts 2-methyl-2-propen-1-ol CC(=C)CO as minor product (see Figure 4) from a parallel decomposition mechanism of the OPO radical via a loss of CO after isomerization of the radical. However, this is it not compatible with the experimental m/z 72 SPES shown in Figure 13, which lacks signal around the first ionization energy of 2-methyl-2-propen-1-ol (9.24 eV)[71]. Additionally, 2-methyl-2-propen-1-ol fragments to give $C_2H_3O^+$ above 9.7 eV. The signal at m/z 43 starts distinctly below 9.5 eV (see Figure S2) with no sign for an additional contribution above 9.7 eV, which confirms the absence of 2-methyl-2-propen-1-ol. The PIMS and GC data in Figure 13 start to disagree at 650 K because the PIMS data are derived from the m/z 72 signal, which does not only originate from 2-methylpropanal but also includes contributions from at least one other species. These species likely have different photoionization cross sections and thus the quantification is questionable.

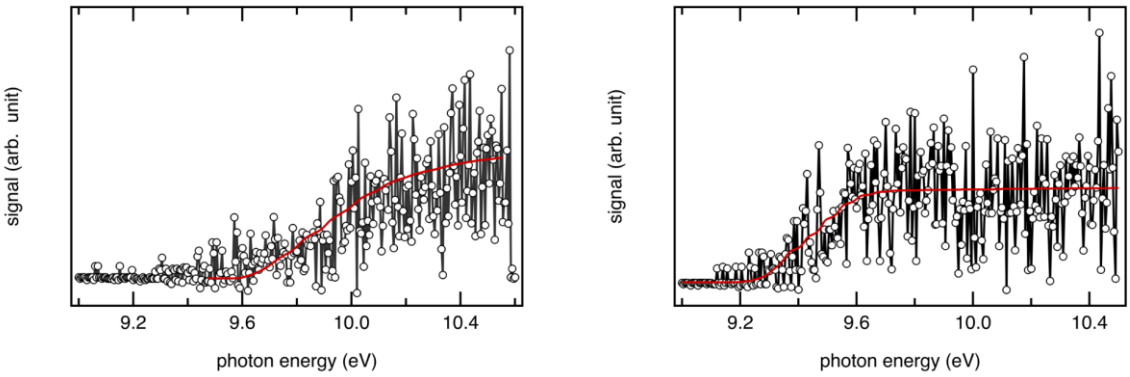

Figure 16. PIY of m/z 102 (left) and 104 (right) registered in PEPICO measurements at 570 K (dots) compared to simulated PIY of 2-methyl-3-methylperoxyprop-1-ene and 1-hydroperoxy-2,2-dimethylpropane (red lines) respectively. Note that the simulated spectra were shifted (see text for explanation).

Tert-butylhydroperoxide CC(C)(C)OO (tBuOOH, m/z 90) is predicted by the kinetic model but not detected in this work. The ionization threshold observed in the PIY of m/z 90 (see right panel in Figure 8), identified as the main KHP fragment, does not coincide with the one of tBuOOH[72]. The kinetic model also predicts that a minor fraction of ROO may be consumed by disproportionation with an HO_2 radical to form 1-hydroperoxy-2,2-dimethylpropane (CC(C)(C)COO, m/z 104) and an O_2 molecule. A signal was recorded at m/z 104 in both NSRL and SOLEIL experiments (see Figure 9). However, the signal of m/z 104 obtained with the PIMS setup does not have the temperature dependence expected for an intermediate. The PIY of m/z 104 recorded in i²PEPICO compared to simulated PIY of 1-hydroperoxy-2,2-dimethylpropane would support this statement though (see right panel in Figure 16). However, the simulated PIY requires an excessively large energy shift (450 meV) to match the PIY curve. Finally, a peak at m/z 102 is also observed in the PEPICO but not in the PIMS mass spectrum (see Figure 9). The kinetic model predicts the formation of 2-methyl-3-methylperoxyprop-1-ene CC(=C)COOC with a maximum mole fraction of 3.5 ppm at 600 K by radical reaction iC_4H_7 + CH_3OO. iC_4H_7 is formed by H-abstraction from isobutene and CH_3OO by O_2-addition on a methyl radical. The PIY of m/z 102 obtained in PEPICO measurements agrees well with the simulated spectrum of 2-methyl-3-methylperoxyprop-1-ene (see left panel in Figure 16). However, as for m/z 104 an excessively large energy shift (600 meV) to match the PIY curve is required.

Chemistry from KHP decomposition products

Other species were detected and quantified by GC and PIMS. Propene (C_3H_6, m/z 42) was quantified by raw mass separation due to a high mass resolving power at NSRL and its experimental mole fraction is in good agreement with the numerical predictions (see left panel of Figure 17). Propene is produced according to the model from 2-methylpropanal, which reacts by H-abstraction with OH followed by CO elimination and H atom loss. Subsequent reaction of propene leads to acetaldehyde (CH_3CHO, m/z 44), for which experimental measurements and numerical predictions of the mole fraction are in relatively good agreement (see right panel in Figure 17) with those measured by LRGP, while the mole fractions derived from NSRL are two times larger.

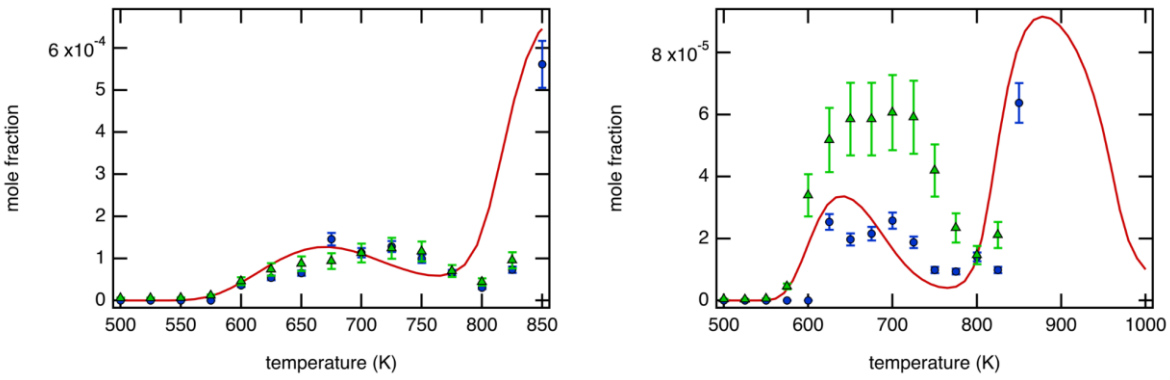

Figure 17. mole fraction of propene (left) and acetaldehyde (right) measured during neopentane oxidation (ϕ = 0.5, 1.5 % in He) at P = 1.07 bar and τ = 3 s. The model prediction is also presented.

The SPES of m/z 42 in the right panel of Figure 18 shows, in addition to propene, the presence of ketene ($H_2C=C=O$), which cannot be detected with good sensitivity by GC. The PES of ketene and propene and the SPES were integrated and normalized. A least-squares fit of the photoelectron spectra of both isomers to the experimental SPES gives an equivalent signal ratio of 0.6:1.0. Relative mole fractions could then be estimated by weighting the branching ratio using the absolute photoionization cross sections at 10.0 eV from Yang et al. for ketene (22.4 Mb)[31] and Person et al. for propene (7.2 Mb)[73]. The weighting leads to a ketene:propene mole fraction (MF) ratio of 0.2:1.0, which is in disagreement with the one derived from simulations. Based on Figure 17 and 18, the predicted ratio would be 0.01:1.0. Since the agreement between the kinetic model and the experiment is good for propene, and using a reference value of 40 ppm for propene at 600 K (see Figure 17), the mole fraction of ketene based on SPES derived MF ratio would be around ~8 ppm. This is in agreement within a factor 2 with the NSRL-derived 4.4 ppm mole fraction at 600 K and shows that the quantification by the SPES method is relatively robust.

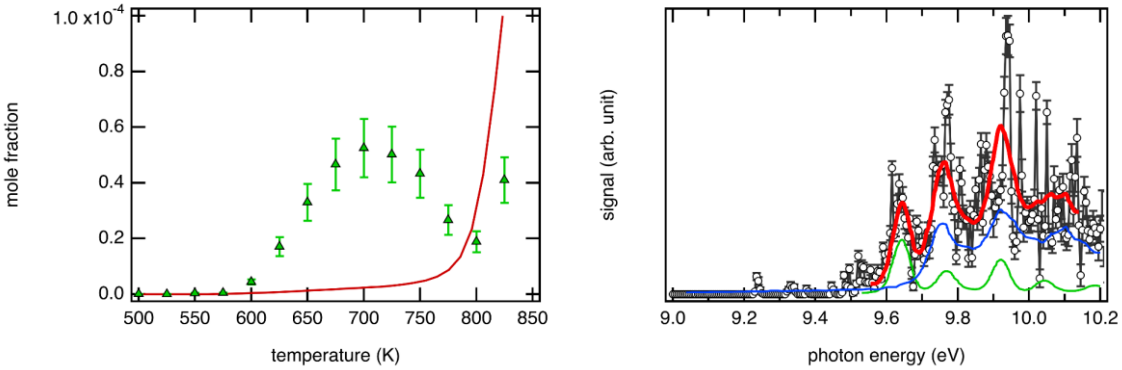

Figure 18. (left) mole fraction of ketene measured during neopentane oxidation (ϕ = 0.5, 1.5 % in He) at P = 1.07 bar and τ = 3 s compared to literature model predictions. (right) SPES of m/z 42 at T = 580 K (dots) compared to PES of ketene (green) from Niu et al.[74] and propene (blue) from Bieri et al.[75] The red curve shows the results of the fit (see text for details).

Finally, methylhydroperoxide (CH_3OOH, m/z 48) has been detected in the PEPICO and PIMS experiments. The SPES of m/z 48 is presented on the right side of Figure 19 and shows a good agreement with the SPES of CH_3OOH obtained during the oxidation of n-pentane at low temperature by Bourgalais et al.[26]. According to the kinetic model, CH_3OOH is produced from the reaction $CH_3OO + HO_2$, with CH_3OO being formed by the addition of an oxygen molecule to a methyl radical. The mole fraction calculated from the PIMS measurements show that this pathway is overestimated by the kinetic model.

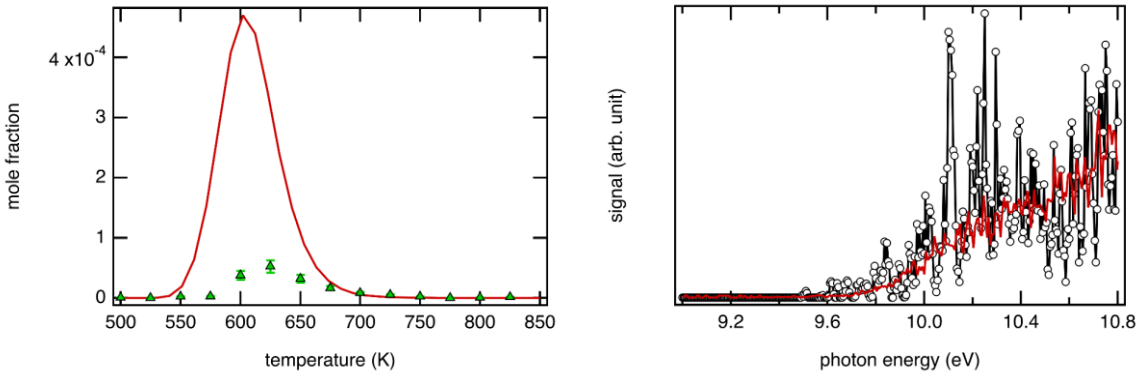

Figure 19. (left) Mole fraction of methylhydroperoxide measured during neopentane oxidation (ϕ = 0.5, 1.5 % in He) at P = 1.07 bar and τ = 3 s compared to literature model predictions. (right) SPES of m/z 48 at T = 580 K (dots) compared to SPES of methylhydroperoxide from Bourgalais et al.[26] (red line).

Conclusion and perspectives

Neopentane oxidation was studied in three JSR experiments in a temperature range from 500 to 850 K, a pressure of 1.07 bar, and for ϕ = 0.5. The products were identified and quantified by several analytical techniques: GC-TCD/FID/MS, SVUV-PIMS, and SVUV-PEPICO. Theoretical calculations were performed to support the assignment of SPES. The use of different techniques provided complementary and coherent results, which increased the confidence in the assignments and quantifications of intermediates. The major first and second O_2 addition products were observed in agreement with the literature: 3,3-dimethyloxetane, 2-methylpropanal, methacrolein, acetone, and isobutene. The KHP was detected and quantified and a fragment of its photoionization at m/z 90 was observed.

Simulations using the kinetic model by Bugler et al.[11] from the literature developed for the oxidation of pentane isomers at low temperature were compared to the experimental results. Disregarding a systematic temperature shift of the predictions, most of the mole fraction profiles are relatively well reproduced, demonstrating the robustness of the kinetic model. Within uncertainties, PIMS and GC mole fractions are in relatively good agreement except for CH_2O for which a significant difference between the mole fractions was observed between PIMS and GC measurements. Both measurements were repeated and appeared very reproducible. The unexpected large presence of formic acid might have caused some CH_2O to polymerize in the GC transfer line. Considering the differences for all aldehydes even taking into account uncertainty, a polymerization effect on this class of compound cannot be excluded at this point. Additional measurements with other analytical tools would be necessary in the future to obtain the accurate mole fraction profiles required for the improvement of the kinetic model. Calibration with known gas quantities at all three sites would be necessary in the future to benchmark the measured mole fraction at the different facilities at the same conditions.

A few significant discrepancies between experimental and predicted mole fractions are observed and related to the possibility that the model is incomplete. The PEPICO measurements indicate the formation of 2,2-dimethylpropanal which is a product not predicted by the kinetic model and not detected by PIMS or GC. However, it was detected by Eskola et al.[17]. The seemingly contradicting results are explained by the fact that 2,2-dimethylpropanal is mainly formed at low temperatures while its isomer 3,3-dimethyloxetane dominates at higher temperatures. In order to confirm this explanation, the photoionization

cross section of 2,2-dimethylpropanal is required for quantification. Furthermore, the relative yields of both isomers should be confirmed since Eskola et al.[17] initiated neopentane oxidation with Cl atoms. The most likely pathways for 2,2-dimethylpropanal formation should be added to the kinetic model to be able to compare experimental and predicted 2,2-dimethylpropanal yields and to find optimized conditions to attempt its detection by GC. A potential pathway to consider would be successive reactions of H-migration from the ROO radical. This would impact the chemistry of the first oxygen addition and the formation of some hydroperoxides that are predicted by the kinetic model but not observed in this work (tBuOOH, 1-hydroperoxy-2,2-dimethylpropane) or overestimated (CH_3OOH).

The formation of KHP could be observed directly in the m/z 118 parent ion channel at the NSRL and indirectly in the m/z 90 dissociative ionization channels at SOLEIL—and the temperature profile is similar to that predicted by the kinetic model. Information on the photoionization cross section is needed in order to compare measured and calculated KHP mole fractions. The decomposition pathways of KHP need to be thoroughly revised in an improved kinetic model. The detection of a signal at m/z 100 shows that it is necessary to consider the possibility of the formation of 2,2-dimethylpropanedial by H_2O-elimination from the KHP. More importantly, the underestimation of the mole fraction measurements of 2-methylpropanal in conjunction with the observation of peaks at m/z 46 assigned to formic acid respectively, highlights the importance of the Korcek reaction, which is not included in the kinetic model.

Besides the Korcek model, the implementation of the isobutene + HO_2 chemistry should be double-checked as it could be an important source of 2,2-dimethyloxirane which was detected in this work but not quantified. Discrepancies in the measured and simulated mole fractions of intermediate yielded by specific pathways, such as γ-KHP decomposition and Korcek reaction, demonstrate that a careful revision of the kinetic model is needed. Development of the kinetic model would benefit from additional experiments with a better sensitivity to provide robust structural information (e.g. m/z 88, 100, 102, 104) and from additional photoionization cross section information (m/z 86, 100, and 118).

Acknowledgement

We are grateful to the whole SOLEIL staff for smoothly running the facility under project 20180021. We warmly thank J-F Gil for his technical help around the SAPHIRS experiment. HHC acknowledges I3A for the use of its HPC cluster HERMES and the funding from the Aragón Government (Ref. T22_20R), co-funded by FEDER 2014-2020 "Construyendo Europa desde Aragón".

References

(1) Wang, Z.; Herbinet, O.; Hansen, N.; Battin-Leclerc, F. Exploring Hydroperoxides in Combustion: History, Recent Advances and Perspectives. *Prog. Energy Combust. Sci.* 2019, *73*, 132–181.

(2) Marshall, R. M.; Purnell, H.; Storey, P. D. Chain Initiation of Neopentane Pyrolysis and a Suggested Reconciliation of the Thermochemically Calculated and Measured Rate Constants for the Recombination of T-Butyl Radicals. *J. Chem. Soc. Faraday Trans. 1 Phys. Chem. Condens. Phases* 1976, *72*, 85–92.

(3) Baronnet, F.; Dzierzynski, M.; Come, G. M.; Martin, R.; Niclause, M. The Pyrolysis of Neopentane at Small Extents of Reaction. *Int. J. Chem. Kinet.* 1971, *3* (3), 197–213.

(4) Baker, R. R.; Baldwin, R. R.; Walker, R. W. The Formation of Acetone in the

Oxidation of Neopentane. *Combust. Flame* 1970, *14* (1), 31–36.
(5) Baker, R. R.; Baldwin, R. R.; Everett, C. J.; Walker, R. W. The Addition of Neopentane to Slowly Reacting Mixtures of Hydrogen and Oxygen at 480 C—I: Formation of Primary Products from Neopentane. *Combust. Flame* 1975, *25*, 285–300.
(6) Baker, R. R.; Baldwin, R. R.; Walker, R. W. Addition of Neopentane to Slowly Reacting Mixtures of H2+ O2 at 480° C. Part II. The Addition of the Primary Products from Neopentane, and the Rate Constants for H and OH Attack on Neopentane. *Combust. Flame* 1976, *27*, 147–161.
(7) Baldwin, R. R.; Hisham, M. W.; Walker, R. W. Arrhenius Parameters of Elementary Reactions Involved in the Oxidation of Neopentane. *J. Chem. Soc. Faraday Trans. 1 Phys. Chem. Condens. Phases* 1982, *78* (5), 1615–1627.
(8) Bradley, J. N.; West, K. O. Single-Pulse Shock Tube Studies of Hydrocarbon Pyrolysis. Part 5.—Pyrolysis of Neopentane. *J. Chem. Soc. Faraday Trans. 1 Phys. Chem. Condens. Phases* 1976, *72*, 8–19.
(9) Rao, V. S.; Skinner, G. B. Further Experiments on Pyrolysis of 2, 2-dimethylpropane behind Shock Waves. *Int. J. Chem. Kinet.* 1988, *20* (2), 165–175.
(10) Bugler, J.; Somers, K. P.; Silke, E. J.; Curran, H. J. Revisiting the Kinetics and Thermodynamics of the Low-Temperature Oxidation Pathways of Alkanes: A Case Study of the Three Pentane Isomers. *J. Phys. Chem. A* 2015, *119* (28), 7510–7527.
(11) Bugler, J.; Marks, B.; Mathieu, O.; Archuleta, R.; Camou, A.; Grégoire, C.; Heufer, K. A.; Petersen, E. L.; Curran, H. J. An Ignition Delay Time and Chemical Kinetic Modeling Study of the Pentane Isomers. *Combust. Flame* 2016, *163*, 138–156.
(12) Ribaucour, M.; Minetti, R.; Sochet, L. R.; Curran, H. J.; Pitz, W. J.; Westbrook, C. K. Ignition of Isomers of Pentane: An Experimental and Kinetic Modeling Study. *Proc. Combust. Inst.* 2000, *28* (2), 1671–1678. https://doi.org/10.1016/S0082-0784(00)80566-4.
(13) Pacey, P. D.; Wimalasena, J. H. Kinetic Study of the Pyrolysis of Neopentane during Its Induction Period. *J. Phys. Chem.* 1980, *84* (18), 2221–2225.
(14) Wang, S.; Miller, D. L.; Cernansky, N. P.; Curran, H. J.; Pitz, W. J.; Westbrook, C. K. A Flow Reactor Study of Neopentane Oxidation at 8 Atmospheres: Experiments and Modeling. *Combust. Flame* 1999, *118* (3), 415–430.
(15) DeSain, J. D.; Klippenstein, S. J.; Taatjes, C. A. Time-Resolved Measurements of OH and HO 2 Product Formation in Pulsed-Photolytic Chlorine Atom Initiated Oxidation of Neopentane. *Phys. Chem. Chem. Phys.* 2003, *5* (8), 1584–1592.
(16) Petway, S. V.; Ismail, H.; Green, W. H.; Estupiñán, E. G.; Jusinski, L. E.; Taatjes, C. A. Measurements and Automated Mechanism Generation Modeling of OH Production in Photolytically Initiated Oxidation of the Neopentyl Radical. *J. Phys. Chem. A* 2007, *111* (19), 3891–3900.
(17) Eskola, A. J.; Antonov, I. O.; Sheps, L.; Savee, J. D.; Osborn, D. L.; Taatjes, C. A. Time-Resolved Measurements of Product Formation in the Low-Temperature (550–675 K) Oxidation of Neopentane: A Probe to Investigate Chain-Branching Mechanism. *Phys. Chem. Chem. Phys.* 2017, *19* (21), 13731–13745.
(18) Dagaut, P.; Cathonnet, M. Oxidation of Neopentane in a Jet-Stirred Reactor from 1 to 10 Atm: An Experimental and Detailed Kinetic Modeling Study. *Combust. Flame* 1999, *118* (1–2), 191–203.
(19) Marquaire, P. M.; Côme, G. M. Non Quasi-Stationary State Pyrolysis. Induction Period of Neopentane Pyrolysis. *React. Kinet. Catal. Lett.* 1978, *9* (2), 165–169.
(20) Hansen, N.; Kukkadapu, G.; Chen, B.; Dong, S.; Curran, H. J.; Taatjes, C. A.; Eskola, A. J.; Osborn, D. L.; Sheps, L.; Pitz, W. J. The Impact of the Third O2 Addition Reaction Network on Ignition Delay Times of Neo-Pentane. *Proc. Combust. Inst.* 2021, *38* (1), 299–307.

*corresponding author: jeremy.bourgalais@univ-lorraine.fr

(21) Sun, H.; Bozzelli, J. W. Thermochemical and Kinetic Analysis on the Reactions of Neopentyl and Hydroperoxy-Neopentyl Radicals with Oxygen: Part I. OH and Initial Stable HC Product Formation. *J. Phys. Chem. A* 2004, *108* (10), 1694–1711.
(22) Curran, H. J.; Pit, W. J.; Westbrook, C. K.; Hisham, M. W. M.; Walker, R. W. An Intermediate Temperature Modeling Study of the Combustion of Neopentane. In *Symposium (International) on Combustion*; Elsevier, 1996; Vol. 26, pp 641–649.
(23) Jalan, A.; Alecu, I. M.; Meana-Pañeda, R.; Aguilera-Iparraguirre, J.; Yang, K. R.; Merchant, S. S.; Truhlar, D. G.; Green, W. H. New Pathways for Formation of Acids and Carbonyl Products in Low-Temperature Oxidation: The Korcek Decomposition of γ-Ketohydroperoxides. *J. Am. Chem. Soc.* 2013, *135* (30), 11100–11114.
(24) Wang, Z.; Herbinet, O.; Cheng, Z.; Husson, B.; Fournet, R.; Qi, F.; Battin-Leclerc, F. Experimental Investigation of the Low Temperature Oxidation of the Five Isomers of Hexane. *J. Phys. Chem. A* 2014, *118* (30), 5573–5594.
(25) Battin-Leclerc, F.; Herbinet, O.; Glaude, P.-A.; Fournet, R.; Zhou, Z.; Deng, L.; Guo, H.; Xie, M.; Qi, F. New Experimental Evidences about the Formation and Consumption of Ketohydroperoxides. *Proc. Combust. Inst.* 2011, *33* (1), 325–331.
(26) Bourgalais, J.; Gouid, Z.; Herbinet, O.; Garcia, G. A.; Arnoux, P.; Wang, Z.; Tran, L.-S.; Vanhove, G.; Hochlaf, M.; Nahon, L. Isomer-Sensitive Characterization of Low Temperature Oxidation Reaction Products by Coupling a Jet-Stirred Reactor to an Electron/Ion Coincidence Spectrometer: Case of n-Pentane. *Phys. Chem. Chem. Phys.* 2020, *22* (3), 1222–1241.
(27) C. Poully, J.; P. Schermann, J.; Nieuwjaer, N.; Lecomte, F.; Grégoire, G.; Desfrançois, C.; A. Garcia, G.; Nahon, L.; Nandi, D.; Poisson, L.; Hochlaf, M. Photoionization of 2-Pyridone and 2-Hydroxypyridine. *Phys. Chem. Chem. Phys.* 2010, *12* (14), 3566–3572. https://doi.org/10.1039/B923630A.
(28) Briant, M.; Poisson, L.; Hochlaf, M.; de Pujo, P.; Gaveau, M.-A.; Soep, B. Ar2 Photoelectron Spectroscopy Mediated by Autoionizing States. *Phys. Rev. Lett.* 2012, *109* (19), 193401. https://doi.org/10.1103/PhysRevLett.109.193401.
(29) Battin-Leclerc, F.; Bourgalais, J.; Gouid, Z.; Herbinet, O.; Garcia, G.; Arnoux, P.; Wang, Z.; Tran, L.-S.; Vanhove, G.; Nahon, L. Chemistry Deriving from OOQOOH Radicals in Alkane Low-Temperature Oxidation: A First Combined Theoretical and Electron-Ion Coincidence Mass Spectrometry Study. *Proc. Combust. Inst.* 2021, *38* (1), 309–319.
(30) Chen, B.; Wang, Z.; Wang, J.-Y.; Wang, H.; Togbé, C.; Alonso, P. E. Á.; Almalki, M.; Mehl, M.; Pitz, W. J.; Wagnon, S. W.; Zhang, K.; Kukkadapu, G.; Dagaut, P.; Mani Sarathy, S. Exploring Gasoline Oxidation Chemistry in Jet Stirred Reactors. *Fuel* 2019, *236*, 1282–1292. https://doi.org/10.1016/j.fuel.2018.09.055.
(31) Yang, B.; Wang, J.; Cool, T. A.; Hansen, N.; Skeen, S.; Osborn, D. L. Absolute Photoionization Cross-Sections of Some Combustion Intermediates. *Int. J. Mass Spectrom.* 2012, *309*, 118–128. https://doi.org/10.1016/j.ijms.2011.09.006.
(32) Rafn Hrodmarsson, H.; A. Garcia, G.; Nahon, L.; Loison, J.-C.; Gans, B. The Absolute Photoionization Cross Section of the Mercapto Radical (SH) from Threshold up to 15.0 EV. *Phys. Chem. Chem. Phys.* 2019, *21* (46), 25907–25915. https://doi.org/10.1039/C9CP05809E.
(33) Hrodmarsson, H. R.; Loison, J.-C.; Jacovella, U.; Holland, D. M. P.; Boyé-Péronne, S.; Gans, B.; Garcia, G. A.; Nahon, L.; Pratt, S. T. Valence-Shell Photoionization of C_4H_5: The 2-Butyn-1-Yl Radical. *J. Phys. Chem. A* 2019, *123* (8), 1521–1528. https://doi.org/10.1021/acs.jpca.8b11809.
(34) Tang, X.; Garcia, G. A.; Gil, J.-F.; Nahon, L. Vacuum Upgrade and Enhanced Performances of the Double Imaging Electron/Ion Coincidence End-Station at the Vacuum Ultraviolet Beamline DESIRS. *Rev. Sci. Instrum.* 2015, *86* (12), 123108.

https://doi.org/10.1063/1.4937624.
(35) Garcia, G. A.; Cunha de Miranda, B. K.; Tia, M.; Daly, S.; Nahon, L. DELICIOUS III: A Multipurpose Double Imaging Particle Coincidence Spectrometer for Gas Phase Vacuum Ultraviolet Photodynamics Studies. *Rev. Sci. Instrum.* 2013, *84* (5), 053112. https://doi.org/10.1063/1.4807751.
(36) Garcia, G. A.; Tang, X.; Gil, J.-F.; Nahon, L.; Ward, M.; Batut, S.; Fittschen, C.; Taatjes, C. A.; Osborn, D. L.; Loison, J.-C. Synchrotron-Based Double Imaging Photoelectron/Photoion Coincidence Spectroscopy of Radicals Produced in a Flow Tube: OH and OD. *J. Chem. Phys.* 2015, *142* (16), 164201. https://doi.org/10.1063/1.4918634.
(37) Adamo, C.; Barone, V. Toward Reliable Density Functional Methods without Adjustable Parameters: The PBE0 Model. *J. Chem. Phys.* 1999, *110* (13), 6158–6170. https://doi.org/10.1063/1.478522.
(38) Frisch, M. J.; Trucks, G. W.; Schlegel, H. B.; Scuseria, G. E.; Robb, M. A.; Cheeseman, J. R.; Scalmani, G.; Barone, V.; Petersson, G. A.; Nakatsuji, H.; Li, X.; Caricato, M.; Marenich, A. V.; Bloino, J.; Janesko, B. G.; Gomperts, R.; Mennucci, B.; Hratchian, H. P.; Ortiz, J. V.; Izmaylov, A. F.; Sonnenberg, J. L.; Williams; Ding, F.; Lipparini, F.; Egidi, F.; Goings, J.; Peng, B.; Petrone, A.; Henderson, T.; Ranasinghe, D.; Zakrzewski, V. G.; Gao, J.; Rega, N.; Zheng, G.; Liang, W.; Hada, M.; Ehara, M.; Toyota, K.; Fukuda, R.; Hasegawa, J.; Ishida, M.; Nakajima, T.; Honda, Y.; Kitao, O.; Nakai, H.; Vreven, T.; Throssell, K.; Montgomery Jr., J. A.; Peralta, J. E.; Ogliaro, F.; Bearpark, M. J.; Heyd, J. J.; Brothers, E. N.; Kudin, K. N.; Staroverov, V. N.; Keith, T. A.; Kobayashi, R.; Normand, J.; Raghavachari, K.; Rendell, A. P.; Burant, J. C.; Iyengar, S. S.; Tomasi, J.; Cossi, M.; Millam, J. M.; Klene, M.; Adamo, C.; Cammi, R.; Ochterski, J. W.; Martin, R. L.; Morokuma, K.; Farkas, O.; Foresman, J. B.; Fox, D. J. *Gaussian 16 Rev. C.01*; Wallingford, CT, 2016.
(39) Dunning, T. H. Gaussian Basis Sets for Use in Correlated Molecular Calculations. I. The Atoms Boron through Neon and Hydrogen. *J. Chem. Phys.* 1989, *90* (2), 1007–1023. https://doi.org/10.1063/1.456153.
(40) Kendall, R. A.; Dunning, T. H.; Harrison, R. J. Electron Affinities of the First-row Atoms Revisited. Systematic Basis Sets and Wave Functions. *J. Chem. Phys.* 1992, *96* (9), 6796–6806. https://doi.org/10.1063/1.462569.
(41) Chai, J.-D.; Head-Gordon, M. Long-Range Corrected Hybrid Density Functionals with Damped Atom–Atom Dispersion Corrections. *Phys. Chem. Chem. Phys.* 2008, *10* (44), 6615–6620. https://doi.org/10.1039/B810189B.
(42) Bloino, J.; Biczysko, M.; Crescenzi, O.; Barone, V. Integrated Computational Approach to Vibrationally Resolved Electronic Spectra: Anisole as a Test Case. *J. Chem. Phys.* 2008, *128* (24), 244105. https://doi.org/10.1063/1.2943140.
(43) Bloino, J. General Approach to Compute Vibrationally Resolved One-Photon Electronic Spectra | Journal of Chemical Theory and Computation https://pubs.acs.org/doi/10.1021/ct9006772 (accessed 2021 -06 -07).
(44) Bloino, J. Aiming at an accurate prediction of vibrational and electronic spectra for medium-to-large molecules: An overview - Bloino - 2016 - International Journal of Quantum Chemistry - Wiley Online Library https://onlinelibrary.wiley.com/doi/full/10.1002/qua.25188 (accessed 2021 -06 -07).
(45) Barone, V. Fully Integrated Approach to Compute Vibrationally Resolved Optical Spectra: From Small Molecules to Macrosystems | Journal of Chemical Theory and Computation https://pubs.acs.org/doi/10.1021/ct8004744 (accessed 2021 -06 -07).
(46) Montgomery, J. A.; Frisch, M. J.; Ochterski, J. W.; Petersson, G. A. A Complete Basis Set Model Chemistry. VI. Use of Density Functional Geometries and Frequencies. *J. Chem. Phys.* 1999, *110* (6), 2822–2827. https://doi.org/10.1063/1.477924.
(47) Montgomery, J. A.; Frisch, M. J.; Ochterski, J. W.; Petersson, G. A. A Complete Basis

Set Model Chemistry. VII. Use of the Minimum Population Localization Method. *J. Chem. Phys.* 2000, *112* (15), 6532–6542. https://doi.org/10.1063/1.481224.
(48) Adler, T. B.; Werner, H.-J.; Manby, F. R. Local Explicitly Correlated Second-Order Perturbation Theory for the Accurate Treatment of Large Molecules. *J. Chem. Phys.* 2009, *130* (5), 054106. https://doi.org/10.1063/1.3040174.
(49) Adler, T. B.; Werner, H.-J. Local Explicitly Correlated Coupled-Cluster Methods: Efficient Removal of the Basis Set Incompleteness and Domain Errors. *J. Chem. Phys.* 2009, *130* (24), 241101. https://doi.org/10.1063/1.3160675.
(50) Adler, T. B.; Knizia, G.; Werner, H.-J. A Simple and Efficient CCSD(T)-F12 Approximation. *J. Chem. Phys.* 2007, *127* (22), 221106. https://doi.org/10.1063/1.2817618.
(51) Knizia, G.; Adler, T. B.; Werner, H.-J. Simplified CCSD(T)-F12 Methods: Theory and Benchmarks. *J. Chem. Phys.* 2009, *130* (5), 054104. https://doi.org/10.1063/1.3054300.
(52) Yousaf, K. E.; Peterson, K. A. Optimized Auxiliary Basis Sets for Explicitly Correlated Methods. *J. Chem. Phys.* 2008, *129* (18), 184108. https://doi.org/10.1063/1.3009271.
(53) Werner, H.-J.; Knowles, P. J.; Knizia, G.; Manby, F. R.; Schütz, M. Molpro: A General-Purpose Quantum Chemistry Program Package. *WIREs Comput. Mol. Sci.* 2012, *2* (2), 242–253. https://doi.org/10.1002/wcms.82.
(54) Bugler, J.; Rodriguez, A.; Herbinet, O.; Battin-Leclerc, F.; Togbé, C.; Dayma, G.; Dagaut, P.; Curran, H. J. An Experimental and Modelling Study of N-Pentane Oxidation in Two Jet-Stirred Reactors: The Importance of Pressure-Dependent Kinetics and New Reaction Pathways. *Proc. Combust. Inst.* 2017, *36* (1), 441–448.
(55) Cuoci, A.; Frassoldati, A.; Faravelli, T.; Ranzi, E. Numerical Modeling of Laminar Flames with Detailed Kinetics Based on the Operator-Splitting Method. *Energy Fuels* 2013, *27* (12), 7730–7753.
(56) Cuoci, A.; Frassoldati, A.; Faravelli, T.; Ranzi, E. OpenSMOKE++: An Object-Oriented Framework for the Numerical Modeling of Reactive Systems with Detailed Kinetic Mechanisms. *Comput. Phys. Commun.* 2015, *192*, 237–264.
(57) Lubrano Lavadera, M.; Song, Y.; Sabia, P.; Herbinet, O.; Pelucchi, M.; Stagni, A.; Faravelli, T.; Battin-Leclerc, F.; De Joannon, M. Oscillatory Behavior in Methane Combustion: Influence of the Operating Parameters. *Energy Fuels* 2018, *32* (10), 10088–10099.
(58) Bagheri, G.; Lavadera, M. L.; Ranzi, E.; Pelucchi, M.; Sabia, P.; de Joannon, M.; Parente, A.; Faravelli, T. Thermochemical Oscillation of Methane MILD Combustion Diluted with N2/CO2/H2O. *Combust. Sci. Technol.* 2019, *191* (1), 68–80.
(59) Stagni, A.; Song, Y.; Vandewalle, L. A.; Van Geem, K. M.; Marin, G. B.; Herbinet, O.; Battin-Leclerc, F.; Faravelli, T. The Role of Chemistry in the Oscillating Combustion of Hydrocarbons: An Experimental and Theoretical Study. *Chem. Eng. J.* 2020, *385*, 123401.
(60) Stevens, W. R.; Walker, S. H.; Shuman, N. S.; Baer, T. Dissociative Photoionization Study of Neopentane: A Path to an Accurate Heat of Formation of the t-Butyl Ion, t-Butyl Iodide, and t-Butyl Hydroperoxide. *J. Phys. Chem. A* 2010, *114* (2), 804–810. https://doi.org/10.1021/jp908583j.
(61) Shiromaru, H.; Katsumata, S. Photoelectron Angular Distribution for Jahn-Teller Split Bands of Some Molecules in VUV Photoelectron Spectroscopy. *Bull. Chem. Soc. Jpn.* 1984, *57* (12), 3543–3551. https://doi.org/10.1246/bcsj.57.3543.
(62) Jonas, A. E.; Schweitzer, G. K.; Grimm, F. A.; Carlson, T. A. The Photoelectron Spectra of the Tetrafluoro and Tetramethyl Compounds of the Group IV Elements. *J. Electron Spectrosc. Relat. Phenom.* 1972, *1* (1), 29–66. https://doi.org/10.1016/0368-2048(72)85004-7.
(63) Traeger, J. C. Heat of Formation for the Formyl Cation by Photoionization Mass

Spectrometry. *Int. J. Mass Spectrom. Ion Process.* 1985, *66* (3), 271–282. https://doi.org/10.1016/0168-1176(85)80002-1.
(64) Mintz, D. M.; Kuppermann, A. Photoelectron Spectroscopy of Ethylene, Isobutylene, Trimethylethylene, and Tetramethylethylene at Variable Angle. *J. Chem. Phys.* 1979, *71* (8), 3499–3513.
(65) Baker, A. D.; Baker, C.; Brundle, C. R.; Turner, D. W. The Electronic Structures of Methane, Ethane, Ethylene and Formaldehyde Studied by High-Resolution Molecular Photoelectron Spectroscopy. *Int. J. Mass Spectrom. Ion Phys.* 1968, *1* (4–5), 285–301.
(66) Rennie, E. E.; Boulanger, A.-M.; Mayer, P. M.; Holland, D. M. P.; Shaw, D. A.; Cooper, L.; Shpinkova, L. G. A Photoelectron and TPEPICO Investigation of the Acetone Radical Cation. *J. Phys. Chem. A* 2006, *110* (28), 8663–8675. https://doi.org/10.1021/jp0616866.
(67) Masclet, P.; Mouvier, G. Étude Par Spectrométrie Photoélectronique d'aldéhydes et de Cétones Éthyléniques Conjugués. *J. Electron Spectrosc. Relat. Phenom.* 1978, *14* (2), 77–97. https://doi.org/10.1016/0368-2048(78)85057-9.
(68) Pieper, J.; Schmitt, S.; Hemken, C.; Davies, E.; Wullenkord, J.; Brockhinke, A.; Krüger, J.; Garcia, G. A.; Nahon, L.; Lucassen, A.; Eisfeld, W.; Kohse-Höinghaus, K. Isomer Identification in Flames with Double-Imaging Photoelectron/Photoion Coincidence Spectroscopy (I2PEPICO) Using Measured and Calculated Reference Photoelectron Spectra. *Z. Für Phys. Chem.* 2018, *232* (2), 153–187. https://doi.org/10.1515/zpch-2017-1009.
(69) Watanabe, I.; Yokoyama, Y.; Ikeda, S. Lone Pair Ionization Potentials of Carboxylic Acids Determined by He(I) Photoelectron Spectroscopy. *Bull. Chem. Soc. Jpn.* 1973, *46* (7), 1959–1963. https://doi.org/10.1246/bcsj.46.1959.
(70) Zhou, C.-W. A comprehensive experimental and modeling study of isobutene oxidation | Elsevier Enhanced Reader https://reader.elsevier.com/reader/sd/pii/S0010218016000365?token=A7D3E642C98A505E020C0745D72C01E8703B69A13E2BB9DEAA4065CBBAA5F5FC2C1AB56257191E04C7AAAEEAA48F520C&originRegion=eu-west-1&originCreation=20210916124604 (accessed 2021 -09 -16). https://doi.org/10.1016/j.combustflame.2016.01.021.
(71) Traeger, J. C.; McAdoo, D. J. Decomposition Thresholds and Associated Translational Energy Releases for Eight C4H8O+. Isomers. *Int. J. Mass Spectrom. Ion Process.* 1986, *68* (1), 35–48. https://doi.org/10.1016/0168-1176(86)87066-5.
(72) Nagaoka, S.; Sawada, K.; Fukumoto, Y.; Nagashima, U.; Katsumata, S.; Mukai, K. Mechanism of Prooxidant Reaction of Vitamin E: Kinetic, Spectroscopic, and Ab Initio Study of Proton-Transfer Reaction. *J. Phys. Chem.* 1992, *96* (16), 6663–6668. https://doi.org/10.1021/j100195a027.
(73) Person, J. C.; Nicole, P. P. Isotope Effects in the Photoionization Yields and the Absorption Cross Sections for Acetylene, Propyne, and Propene. *J. Chem. Phys.* 1970, *53* (5), 1767–1774. https://doi.org/10.1063/1.1674254.
(74) Niu, B.; Bai, Y.; Shirley, D. A. High Resolution He Iα Photoelectron Spectroscopy of H2CCO and D2CCO Using Supersonic Molecular Beams. *Chem. Phys. Lett.* 1993, *201* (1), 217–222. https://doi.org/10.1016/0009-2614(93)85059-W.
(75) Bieri, G.; Burger, F.; Heilbronner, E.; Maier, J. P. Valence Ionization Energies of Hydrocarbons. *Helv. Chim. Acta* 1977, *60* (7), 2213–2233. https://doi.org/10.1002/hlca.19770600714.

*corresponding author: jeremy.bourgalais@univ-lorraine.fr